Article

Copper Phosphinate Complexes as Molecular Precursors for Ethanol Dehydrogenation Catalysts

Tomas Pokorny,[||] Iaroslav Doroshenko,[||] Petr Machac, Lucie Simonikova, Miroslava Bittova, Zdenek Moravec, Katerina Karaskova, David Skoda, Jiri Pinkas, and Ales Styskalik*

Read Online

ACCESS | Metrics & More | Article Recommendations | Supporting Information

ABSTRACT: Nowadays, the production of acetaldehyde heavily relies on the petroleum industry. Developing new catalysts for the ethanol dehydrogenation process that could sustainably substitute current acetaldehyde production methods is highly desired. Among the ethanol dehydrogenation catalysts, copper-based materials have been intensively studied. Unfortunately, the Cu-based catalysts suffer from sintering and coking, which lead to rapid deactivation with time-on-stream. Phosphorus doping has been demonstrated to diminish coking in methanol dehydrogenation, fluid catalytic cracking, and ethanol-to-olefin reactions. This work reports a pioneering application of the well-characterized copper phosphinate complexes as molecular precursors for copper-based ethanol

Wet Impregnation
Calcination 500 °C

Ethanol Dehydrogenation

50 nm

Cu-phosphate/SiO$_2$

dehydrogenation catalysts enriched with phosphate groups (**Cu-phosphate/SiO$_2$**). Three new catalysts (**CuP-1**, **CuP-2**, and **CuP-3**), prepared by the deposition of complexes {Cu(SAAP)}$_n$ (**1**), [Cu$_6$(BSAAP)$_6$] (**2**), and [Cu$_3$(NAAP)$_3$] (**3**) on the surface of commercial SiO$_2$, calcination at 500 °C, and reduction in the stream of the forming gas 5% H$_2$/N$_2$ at 400 °C, exhibited unusual properties. First, the catalysts showed a rapid increase in catalytic activity. After reaching the maximum conversion, the catalyst started to deactivate. The unusual behavior could be explained by the presence of the phosphate phase, which made Cu^{2+} reduction more difficult. The phosphorus content gradually decreased during time-on-stream, copper was reduced, and the activity increased. The deactivation of the catalyst could be related to the copper diffusion processes. The most active **CuP-1** catalyst reaches a maximum of 73% ethanol conversion and over 98% acetaldehyde selectivity at 325 °C and WHSV = 2.37 h^{-1}.
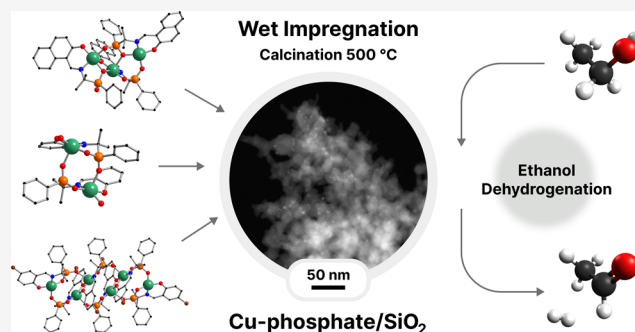
INTRODUCTION

Nowadays, the production of chemical compounds tends to focus on ecology and sustainability.[1,2] Acetaldehyde is a large-scale substance produced worldwide for many applications and as a precursor for further synthesis (acetic acid and ethyl acetate).[3] Current production of acetaldehyde is mainly based on petroleum chemistry.[4−8] First, the ethylene is produced by energetically demanding steam cracking, and then the acetaldehyde is made by the Wacker oxidation using homogeneous catalysts containing heavy metals.[9,10] Non-oxidative dehydrogenation of ethanol to acetaldehyde (the first step of the Lebedev process[11,12]) shows the utilization of bioethanol to produce a variety of sustainable and biobased chemicals.[13,14]

According to the literature reports, copper acts as a highly active and selective ethanol dehydrogenation catalyst.[7] For example, high selectivity to acetaldehyde (up to 100%) has been reported by Chang et al., where rice husk ash (more than 99% SiO$_2$) with copper nanoparticles (1−1.5 nm) were used as catalysts.[15] However, current copper-based catalysts suffer from deactivation by coking and sintering.[14,16−19] Coking has been shown to be one of the deactivation processes in Cu/SiO$_2$

catalysts prepared by dry impregnation, strong electrostatic adsorption, hydrolytic sol−gel, and solvothermal hot injection.[20] Similarly, Pampararo et al. showed carbon deposition on Cu/SiO$_2$ catalysts prepared by aerosol-assisted sol−gel. The more active the catalysts, the higher the amount of carbonaceous materials deposited during the catalytic reaction.[21] In addition to catalyst coking, copper sintering presents a severe problem at higher temperatures. For example, Cu/SiO$_2$ catalysts prepared by incipient wetness impregnation lost half of their activity during 4 h at 300 °C. The deactivation was caused by Cu sintering.[22] Similarly, Cu/SiO$_2$ samples with 0.5 and 1 wt % of copper started losing catalytic activity at 300 °C due to the particle sintering. Surprisingly, smaller particles prepared by the deposition−precipitation method (23 nm) exhibited better catalytic activity and stability than larger particles prepared by
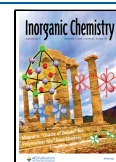
wet impregnation (84 nm).[16] These results suggest that it is crucial to study the stability of copper-based catalysts, describe the sintering and coking in detail, and develop new catalysts based on the gained knowledge.[14,16−19]

Applying molecular precursors to prepare structure-controlled catalysts with homogeneously dispersed catalytic species on the support is a well-known and widely used method.[23−25] However, there is a lack of information on applying phosphorus-containing metal complexes (phosphates, phosphonates, and phosphinates) as precursors to nonoxidative ethanol dehydrogenation catalysts. Numerous studies have been conducted on copper phosphates[26−34] and phosphonates.[35−53] However, the application of phosphinate ligands for the formation of copper complexes has seen limited exploration, with a modest number of copper complexes based on phosphinate ligands present to date.[54−93] A small amount of the copper complexes with macrocyclic ligands possessing pendant phosphinate groups are also being studied for potential medical applications.[94−101] The formation of insoluble polymeric compounds is commonplace in such systems, which is a factor that limits their potential application as molecular precursors. Typical strategies employed for the isolation of molecular species include the utilization of bulky ligands,[34,37] incorporation of additional ancillary ligands,[40,48,49,52,65,73] and the exchange of labile ligands within the molecular clusters (cluster expansion).[51,52,80]

The addition of phosphorus into Cu/SiO_2 catalysts prepared by incipient wetness impregnation and ion-exchange method was studied by Yamamoto et al.[102] Interestingly, phosphorus-containing catalysts exhibited a significant increase in formaldehyde productivity during methanol dehydrogenation. Incorporating phosphorus in Cu/AlPO catalysts is known to influence catalytic activity and stability.[103] Synthesizing alumina modified with phosphorus reduces the amount of coke formation in the methanol-to-dimethyl ether dehydration reaction.[104] Similarly, the addition of phosphorus in the form of phosphate has been reported to lead to a decrease in coke formation in hydrocarbon catalysis and consequently to increased catalytic lifetime.[102] van der Bij et al.[105] and Xia et al.[106] pointed to anticoking properties of phosphorus-doped zeolites.

This work presents the structures of new well-soluble polymer (**1**) and molecular (**2** and **3**) copper phosphinate complexes of various nuclearity, their deposition on porous silica support by wet impregnation followed by thermal decomposition leading to **Cu-phosphate/SiO$_2$** materials, and the catalytic properties of these catalysts in ethanol dehydrogenation. The main goal of the application of the copper phosphinate complexes in wet impregnation was to disperse copper and phosphorus homogeneously on the surface of the SiO_2 matrix. Through the utilization of readily synthesized novel Schiff base phosphinate ligands ($SAAP^{2−}$, $BSAAP^{2−}$, and $NAAP^{2−}$) incorporating additional organic groups featuring donor and ionic functionalities in the process of complex preparation, it becomes possible to produce mainly molecular, highly soluble metallophosphinates. These species possess a predetermined stoichiometric ratio of Cu and P, as well as varying nuclearities that depend on the structure of the ligand. Small and uniform particles containing both Cu and P in equal molar amounts were successfully formed. Interestingly, the materials prepared in such a way exhibited a peculiar catalytic behavior, distinctively different from the benchmark catalysts obtained by the dry impregnation methods with and without the presence of phosphorus. The most active **Cu-phosphate/SiO$_2$** catalyst was analyzed ex-situ by ICP-OES, XPS, and STEM analyses at the different stages of the catalyst lifetime (i.e., after calcination, after H_2 treatment, at the top of catalytic activity, spent catalyst) to gain a deep understanding of the unprecedented catalytic properties.

■ EXPERIMENTAL SECTION

General Procedures. All reactions were performed using general synthetic techniques; no special conditions were used. Commercially available benzyl carbamate (TCI), dichlorophenylphosphine (Sigma), NaOH, salicylaldehyde (Sigma), 5-bromosalicylaldehyde (Sigma), 2-hydroxy-1-naphtalaldehyde (Sigma), methanol-d$_4$ (Sigma), benzene-d$_6$ (TCI), propan-2-ol (p.a.), ethanol (p.a.), methanol (p.a.), acetone (p.a.), pentane (p.a.), acetic acid (p.a.), $Cu(NO_3)_2 \cdot 2.5H_2O$, and Aerosil 300 (Evonik) were used as received.

Caution! *Acute toxic (oral, Cat 3) and corrosive (Sub-Cat 1B) dichlorophenylphosphine; corrosive (Cat 1, Sub-Cat 1A) NaOH; Acute toxic (oral, Cat 4) and aquatic hazard (Cat2) salicylaldehyde; Flammable (Cat 2) and acute toxic (Cat 1, 3) methanol-d4; Flammable (Cat 2), skin and eye irritant (Cat 2), toxic (Cat 1), carcinogenic and mutagenic (Cat 1A, 1B), and aquatic hazard (Cat 3) benzene-d6; Flammable (Cat 2), eye irritant (Cat 2), and specific target organ toxic (Cat 3) propan-2-ol; Flammable (Cat 2) and eye irritant (Cat 2) ethanol; Flammable (Cat 2) and acute toxic (oral, inhalation, and dermal, Cat 3) methanol; Flammable (Cat 2), eye irritant (Cat 2), and specific target organ toxic (Cat 3) acetone; Flammable (Cat 2), specific target organ toxic (Cat 3), aspiration hazardous (Cat 1), and aquatic hazard (Cat 2) pentane; Flammable (Cat 3), corrosive (Sub-Cat 1A), and serious eye damage (Cat 1) acetic acid; Oxidizing (Cat 1), corrosive (Cat 1, Sub-Cat 1B), acute toxic (oral, Cat 4), eye damage (Cat 1), and aquatic hazard (Cat 1) copper nitrate constitute significant safety hazards and must be handled with care and caution.*

Characterization Methods. Elemental maps, nanoparticle size, and distribution were measured by scanning transmission electron microscopy with energy-dispersive X-ray spectroscopy (STEM-EDS) on a Thermo Fisher Scientific Talos F200 instrument equipped with a Bruker X-flash EDS detector. The device operated at 40−200 kV of accelerating potential. The size of the nanoparticles was determined using an ImageJ image processing program.[107] Nanoparticle diameters were measured across the widest side. The surface chemical composition was analyzed by X-ray photoelectron spectroscopy (XPS) on a Kratos Axis Supra device equipped with a monochromatic X-ray source with Al K$_\alpha$ (E = 1486.6 eV) excitation. Binding energy 284.8 eV for C 1s was used for calibration. An Autosorb iQ3 (Quantachrome Instrument) porosimeter was used for measuring the specific surface area by nitrogen adsorption. Both isotherms (adsorption and desorption) were measured at liquid nitrogen temperature (−195.7 °C). Before measurements, samples were degassed at a temperature of 200 °C. BET analysis was used to determine the specific surface area from isotherms measured in the 0.05−0.30 relative pressure range. A Netsch STA 449 Jupiter instrument was used for thermogravimetric (TG) analyses. Samples were heated to 1000 °C in Pt crucibles with a heating rate of 5 °C min^{-1} in a synthetic air atmosphere with a flow of 100 cm^3 min^{-1}. Single-crystal X-ray diffraction measurements were performed on a Rigaku diffraction system (MicroMax007HF DW rotating anode source with multilayer optic, partial χ axis goniometer, Saturn 724+ HG detector, and Cryostream cooling device). The Mo−K$_\alpha$ (λ = 0.7107 Å) radiation was used. Data were corrected for Lorentz and polarization effects; absorption was taken into account on a semiempirical basis using multiple-scans.[108−110] *CrystalClear* (Rigaku 2014) and *CrysAlisPro* (Agilent Technologies 2013) software packages were used for data collection and reduction. The structures were solved using the *SHELXT*[111] program and refined (full matrix least-squares refinement on F_o^2) using the *SHELXL*[112] program. An EMPYREAN instrument from PANalytical was used for powder X-ray diffraction analyses. Samples were placed on a spinning sample bed. The Co K$_\alpha$ radiation (λ = 1.78903 Å) was used (20 mA, 30 kV). A semiconductor detector was used in 1D mode. Also, a MiniFlex 600 instrument by Rigaku was used for powder X-ray diffraction analyses. The Co K$_\alpha$ radiation (λ = 1.78903
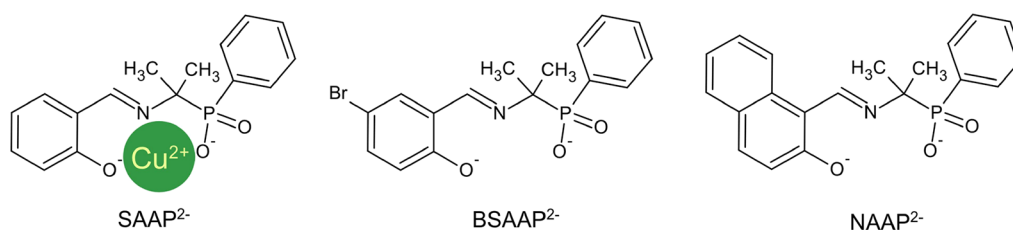
Figure 1. Schematic representation of the L^{2-} ligands used in this study. The green circle schematically depicts the copper(II) atom situated in the coordination pocket of the $SAAP^{2-}$ ligand.

Å) was used (15 mA, 40 kV). Data processing was performed with Rigaku PDXL2 software. Elemental contents were measured by inductively coupled plasma optical emission spectroscopy (ICP-OES). ICP-OES analyses were done on an ICP-OES spectrometer iCAP PRO XPS Duo (Thermo, RF Power 1.10 kW, nebulizer gas flow 0.65 dm^3 min^{-1}, radial viewing high 11.0 mm). Emission lines 177.495, 178.284, and 213.618 nm for P and 324.754 and 327.396 nm for Cu were used. The ESI-MS spectra were measured on an Agilent 6224 Accurate-Mass TOF mass spectrometer (Agilent Technologies, Wilmington, DE, USA) with a dual electrospray ionization source from a methanol solution. The following parameters were used: nitrogen flow 5 L min^{-1}, gas temperature 325 °C, nebulizer 45 psi, skimmer 65 V, and fragmentor 50 and 100 V. IR spectra were recorded on a Bruker Tensor 27 FTIR spectrometer with a Bruker Platinum ATR system. The solution NMR spectra were recorded on a Bruker Avance III 300 NMR spectrometer at frequencies of 300.1 MHz for ^1H and 121.5 MHz for ^{31}P in 5 mm NMR tubes. CD_3OD and C_6D_6 were used as an internal lock. The spectra were referenced to the residual proton signal of CHD_2OD (3.33 ppm) and C_6HD_5 (7.16 ppm), while the ^{31}P spectra were referenced to 85% H_3PO_4 (0 ppm). Hydrogen temperature-programmed reduction (H_2-TPR) was carried out on AutoChem II-2920 equipment (Micromeritics, Atlanta, GA, USA). Before each H_2-TPR experiment, the sample (0.1 g) was pretreated in Ar (50 mL min^{-1}) at 300 °C for 30 min. The sample was cooled to 50 °C in the same atmosphere and then reduced in a hydrogen–argon mixture (10 mol % H_2/Ar) at a flow of 50 mL min^{-1} and constant heating rate of 10 °C min^{-1} up to 500 or 700 °C and held at this temperature for 30 min. The water vapor formed during the TPR measurements was captured in a cold trap. Correction based on the signal of the neat silica support (Aerosil 300) was used for the evaluation of the number of reducible species.

Ligand and Complex Synthesis. Detailed synthetic procedures of (2-{[(E)-(2-hydroxyphenyl)methylidene]amino}propan-2-yl)-phenylphosphinate (HSAAP$^-$), (2-{[(E)-(5-bromo-2-hydroxyphenyl)methylidene]amino}propan-2-yl)phenylphosphinate (HBSAAP$^-$), and (2-{[[(E)-(2-hydroxynaphthalen-1-yl)methylidene]-amino}propan-2-yl)phenylphosphinate (HNAAP$^-$) sodium salts (Figure 1) are described in Supporting Information. Ligands HSAAP$^-$, HBSAAP$^-$, and HNAAP$^-$ were deprotonated and used to prepare copper phosphinate complexes {Cu(SAAP)}$_n$, (1), [Cu$_6$(BSAAP)$_6$] (2), and [Cu$_3$(NAAP)$_3$] (3). Synthesis details and characterization are described in Tables S1–S3. Copper phosphinate complexes 1–3 were used as precursors for catalyst preparation (see below).

Catalyst Preparation. CuP-1–3 and CuP-3-TEP (10-fold loading of Cu) catalysts were prepared by the wet impregnation of the corresponding complex 1–3 on the commercial SiO$_2$ support (Aerosil 300) from MeOH solution (50 cm^3). After Aerosil was added to a clear solution of a complex, the suspension was sonicated for 5 min for homogenization and then evaporated on a rotary evaporator. The well-dried, homogeneously green sample was calcined in air for 10 h at 500 °C, resulting in a light-blue product. The weight of the complex and support was calculated to obtain 2.5 wt % Cu loading for CuP-1–3 and 25 wt % Cu loading for CuP-3-TEP (masses used in the preparation are summarized in Table S4). The Cu-DI benchmark catalyst was prepared by the previously reported procedure.[20] Cu(NO$_3$)$_2$·2.5H$_2$O (91.5 mg, 0.393 mmol) was dissolved in water (10 cm^3) and mixed with silica (Aerosil 300, 1.0 g) to form a paste. The sample was dried in an oven at

70 °C with occasional mixing. The dried catalyst was ground and calcined at 500 °C for 5 h. The CuP-Y benchmark catalyst was prepared according to the previously reported procedure[102] by the dry impregnation method. Cu(NO$_3$)$_2$·2.5H$_2$O (188 mg, 0.808 mmol) was dissolved in water (20 cm^3) and mixed with silica (Aerosil 300, 2.0 g) to form a paste. The sample was dried in an oven at 100 °C with occasional mixing. Then a solution of 85% H$_3$PO$_4$ (0.093 g, 0.807 mmol) in 10 cm^3 of water was added, and the sample was mixed well and dried at 100 °C with occasional mixing. The dried catalyst was ground and calcined at 500 °C for 10 h. The CuP-P benchmark catalyst was prepared by the addition of a solution of (NH$_4$)$_2$HPO$_4$ (0.053 g, 0.401 mmol) in 25 cm^3 of water to a suspension of silica (Aerosil 300, 1.0 g) in a solution of Cu(NO$_3$)$_2$·2.5H$_2$O (0.094 g, 0.404 mmol) in methanol (25 cm^3). The mixture was then sonicated for a few minutes to ensure proper homogenization. After sonication, the suspension was dried using a rotary evaporator and then calcined at 500 °C for 10 h.

Catalytic Reactor Details. For catalysis, a fixed-bed catalytic reactor was used. Gas chromatography with a flame ionization detector was used to determine the catalytic activity. Catalytic tests were performed at 325 °C for up to 50 h. The effluent gas analysis was carried out by an HP 6890 Gas Chromatograph equipped with a flame ionization detector and a Thermo scientific TG-BOND U column (length of 30 m, internal diameter of 0.32 mm, and film thickness of 10 μm). Calcined catalysts (200 mg) with selected grain size (0.2–0.4 mm) were diluted with glass beads (0.5–1 mm) to a constant volume. The void space in the reactor tube was filled with glass beads. Before the reaction, the catalysts were pretreated in situ by feeding hydrogen (10 vol % H$_2$ in N$_2$) for 1 h at 400 °C (Cu reduction). During all processes, nitrogen was used as carrier gas (50 cm^3 min^{-1}); ethanol was fed by a NE-300 syringe pump with WHSV 2.37 h^{-1} (7.7 mol % ethanol in N$_2$). Pentane was added as the internal standard (5% molar concentration in ethanol feed). The tests were carried out at atmospheric pressure.

RESULTS AND DISCUSSION

Cu(II) Phosphinate Complex Synthesis and Structure. The reactions between the ligands SAAP^{2-}, BSAAP^{2-}, and NAAP^{2-} (Figure 1) in the methanolic solution with the equimolar amount of the Cu(NO$_3$)$_2$·2.5H$_2$O and sodium hydroxide lead to three new Cu(II) phosphinate complexes. The obtained compounds were isolated from the byproducts by the dissolution of the dried reaction mixture in THF, filtration, drying, and crystallization of the pure products from acetonitrile solutions. Detailed synthetic procedures and the characterization of the ligands and complexes are described in the Supporting Information.

The single crystals were obtained for all three Cu(II) phosphinate complexes, and molecular structure models were obtained by single-crystal X-ray diffraction. Complex 1 crystallizes as a 1D polymer with the repeating formula unit {Cu(SAAP)}$_n$ in the monoclinic $P2/c$ space group, while compounds 2 and 3 crystallize in the triclinic $P\bar{1}$ space group and remain in the molecular form with the formulas [Cu$_6$(BSAAP)$_6$] and [Cu$_3$(NAAP)$_3$], respectively. The main crystallographic and refinement parameters are summarized in Table S1. For all three

structures, the primary trend is that Cu^{2+} cations are coordinated in the ONO coordination pocket of the ligands (Figure 1).

Further coordination and final arrangement of the Cu(II) phosphinate complexes are driven by steric differences in the ligand molecules. The polymeric structure of **1** could be described as binuclear units $Cu_2(SAAP)_2$, consisting of two Cu(SAAP) moieties interconnected to the cycle by the second phosphinic oxygen (not involved in the ONO coordination pocket) with a formation of two Cu−OPO−Cu bridges. The units are connected to the polymer chain by mutual coordination of copper(II) atoms by phenolic oxygen atoms. All copper(II) atoms in the structure of **1** are crystallographically equivalent and five-coordinated by the ONO pocket atoms, one phosphinic, and one phenolic oxygen atom from two other ligands, as depicted in Figure 2 (coordination polyhedra will be discussed below). The closest distance between the copper(II) atoms is equal to 3.059 Å in the phenoxy-bridged Cu_2O_2 moiety.
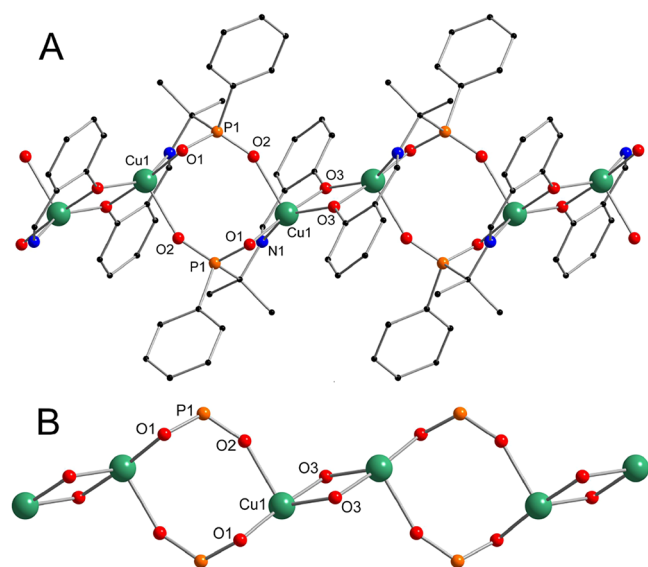

Figure 2. Ball and stick representation of the structure of **1**. The complete chain structure (A) and phosphinate cores connected by the phenolic oxygen bridges (B). Color code: Cu green, P orange, O red, N blue, and C black. Hydrogen atoms have been omitted for the sake of clarity.

In the case of **2**, the formation of the centrosymmetric hexanuclear complex was observed. The whole molecular motive is more complicated than that of other complexes (Figure 3). Three independent copper(II) atom centers of the molecule are four- (Cu1) and five-coordinated (Cu2 and Cu3). The coordination environments of copper(II) atoms are based on an ONO coordination pocket and are completed by a phosphinic oxygen atom of another ligand (Cu1) and one phosphinic and one phenolic oxygen atom from two other ligands (Cu2 and Cu3), as depicted in Figure 3. All copper(II) atoms are situated on the same plane. The closest distance of 3.019 Å was observed between Cu2 and Cu3 atoms in phenoxy-bridged Cu_2O_2 moieties similar to that of copper phosphinate **1**.

The structure of trinuclear molecular complex **3** is similar to the structure of **2** if it is cut in half. In correspondence to **2**, Cu1 is four-coordinated, while Cu2 and Cu3 are five-coordinated. The main difference is that in **2**, the Cu2 and Cu3 atoms are connected by two phenolic oxygen bridges, while in **3**, they are connected by one phenolic and one phosphinic oxygen bridge.
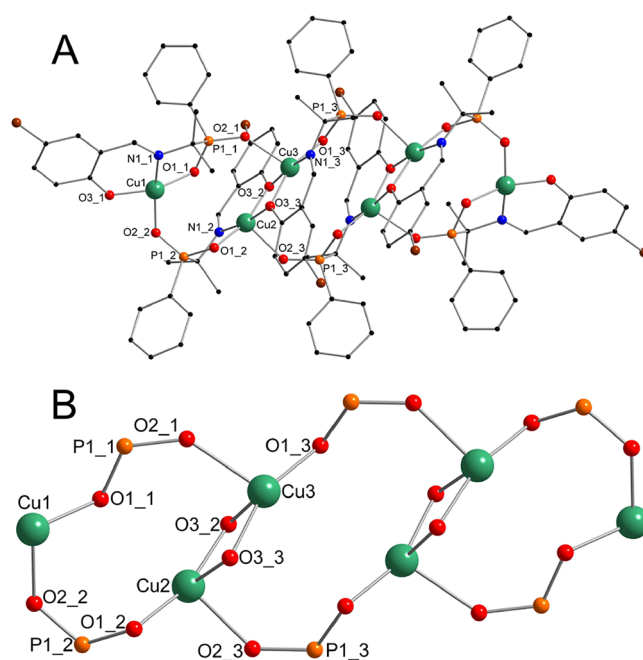

Figure 3. Ball and stick representation of the structure of **2**. The models of the molecule (A) and the core only (B). Color code: Cu green, P orange, O red, N blue, C black, and Br brown. Hydrogen atoms were omitted for the sake of clarity.

This, combined with the steric effect of the ligand, results in a larger distance between Cu2 and Cu3 atoms, reaching 3.115 Å (Figure 4).
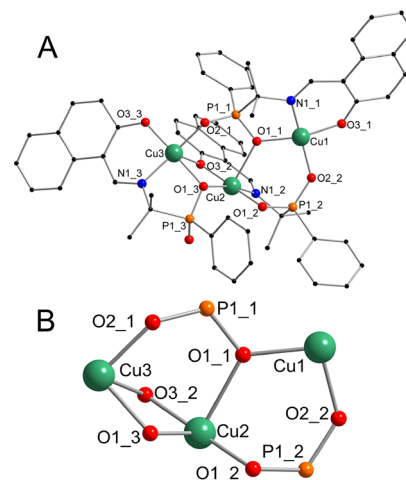

Figure 4. Ball and stick representation of the structure of **3**. The model of the molecule (A) and the core only (B). Color code: Cu green, P orange, O red, N blue, and C black. Hydrogen atoms were omitted for the sake of clarity.

Selected bond lengths in the Cu polyhedra are summarized in Table S2. Continuous shape measures (CShM)[113−116] of the copper(II) atoms polyhedra for the formed complexes **1−3** showed that the geometry of five-coordinated polyhedra is closer to the square pyramidal in all cases than to trigonal bipyramidal with the distortion values in the range of 0.726−2.550 (see Table S3). The polyhedra of the four-coordinated Cu^{2+} cations in complexes **2** and **3** are closer to square than tetrahedral geometry (see Table S3).

Table 1. Experimental Cu and P Loadings in Catalysts (ICP-OES)

sample	precursor	Cu loading [wt %]	P loading [wt %]	Cu:P mol ratio
CuP-1	$\{Cu(SAAP)\}_n$ (**1**)	1.79	0.93	0.93
CuP-2	$[Cu_6(BSAAP)_6]$ (**2**)	2.33	1.13	1.0
CuP-3	$[Cu_3(NAAP)_3]$ (**3**)	1.76	0.85	1.0
Cu-DI	$Cu(NO_3)_2 \cdot 2.5H_2O$	2.42		
CuP-Y	$Cu(NO_3)_2 \cdot 2.5H_2O + H_3PO_4$	2.19	1.11	0.96
CuP-P	$Cu(NO_3)_2 \cdot 2.5H_2O + (NH_4)_2HPO_4$	2.25	1.12	0.97

The molecular nature of the dissolved complexes **1**−**3** used in the catalyst preparation was confirmed through the study of their methanolic solutions by ESI-MS spectroscopy. The spectra were recorded in positive and negative modes under different conditions. The coordination polymer **1** exhibited the presence of small molecular clusters with nuclearity ranging from 2 to 5 when the fragmentor voltage was set to 100 V. When 50 V was applied, the most intense peaks corresponded to four and five nuclear fragments (Figures S1 and S2). The spectra of the hexanuclear complex **2**, recorded with fragmentor voltages of 50 and 100 V, displayed similar patterns, showing the parent peak $[Cu_6(BSAAP)_6 + H]^+$ with a relative intensity of ~4%. The presence of smaller fragments containing 5 to 2 Cu atoms with higher intensities confirms the fragmentation of the molecule during the ionization process (Figures S3 and S4). The spectra of trinuclear complex **3**, recorded with a fragmentor voltage of 100 V, predominantly exhibited the molecular parent peaks ($[Cu_3(NAAP)_3 + H]^+$ and $[Cu_3(NAAP)_3 + Na]^+$) when a lower concentration of the sample was used (Figure S5). Furthermore, alongside the parent peaks, the spectra displayed aggregation into larger species containing 4 and 5 Cu atoms when a higher concentration of the sample was employed (Figure S6). The spectra recorded in negative ion mode do not provide significant information, as larger fragmentation occurs for all complexes and the peaks of lower nuclearity are predominantly observed (Figures S2, S4, and S6).

The behavior of Cu(II) phosphinate complexes **1**−**3** upon heating was analyzed by the TG/DSC method (Figures S7−S9). Complexes **1** and **3** showed thermal stability up to 250 °C, while complex **2** was stable practically to 300 °C. Above these temperatures, continuous weight losses were observed until 800 °C. The residual masses at 1000 °C were 40.21, 28.90, and 33.91 wt % for **1**−**3**, respectively.

Complexes **1**−**3** calcined at 500 °C (5 °C min^{-1}, air, 10 h) and 1000 °C (5 °C min^{-1}, air, no dwell) were studied by powder X-ray diffraction analysis (PXRD). The predominant phase observed in all samples calcined at 500 °C is copper diphosphate $Cu_2P_2O_7$ (PDF: 00−044−0182)[117,118] (Figure S10). Additionally, the presence of an intense diffraction around 10° 2Θ points to the presence of an additional phase of hydrated copper diphosphate $Cu_2P_2O_7 \cdot 3H_2O$ (PDF: 00−051−0202)[119] (Figure S10). Partial hydration could occur due to the samples being exposed to atmospheric moisture during the time between calcination and PXRD analysis. The primary phase observed in samples calcined at 1000 °C remains $Cu_2P_2O_7$ (PDF: 00−044−0182)[117,118] (Figure S11). However, there is an increasing presence of the $Cu_3(PO_4)_2$ phase (PDF: 00−080−0992)[120] content in the succession of calcined complexes from **1** to **3** (Figure S11).

The absorption bands typical for phosphate group vibrations were observed in the IR spectra of Cu(II) phosphinate complexes after calcination at 500 °C for 10 h. Also, no absorption bands of the C−H stretches were observed in the

2800−3000 cm^{-1} region (Figure S12). Therefore, the temperature of 500 °C and 10 h calcination time were applied in the catalyst preparation (see the Synthesis and Characterization of Cu-Phosphate/SiO2 Catalysts section).

Synthesis and Characterization of Cu-Phosphate/SiO$_2$ Catalysts. Three Cu(II) phosphinate complexes **1**−**3** were used as precursors for copper and phosphorus deposition on porous commercial SiO$_2$ by wet impregnation to prepare the **Cu-phosphate/SiO$_2$** catalysts (**CuP-1**−**3**). A benchmark sample without phosphorus was prepared by the dry impregnation method similar to a promising Cu/SiO$_2$ ethanol dehydrogenation catalyst working at 325 °C (**Cu-DI**).[20] A benchmark catalyst containing phosphorus was prepared using two methods. The **CuP-Y** catalyst was prepared using the method described by Yamamoto et al.,[102] employing the dry impregnation technique. On the other hand, the **CuP-P** catalyst was prepared through precipitation of CuHPO$_4$ in the silica suspension. Experimental loadings of Cu and P in the catalysts after calcination are summarized in Table 1. Cu contents in the **Cu-phosphate/SiO$_2$** catalysts were in the range of 1.76 to 2.33 wt %. The atomic Cu:P ratios were close to 1:1 in all three catalysts and thus followed the atomic Cu:P ratios in the starting Cu(II) phosphinate precursors. The benchmark catalysts containing phosphorus exhibited the same Cu:P ratio (close to 1:1).

All catalysts were prepared using the same silica support Aerosil 300 (284 m^2 g^{-1}, 1.55 cm^3 g^{-1}, isotherm shown in Figure S13). The porosity of **Cu-phosphate/SiO$_2$** samples was very similar to that of the catalyst support and the **Cu-DI**, **CuP-Y**, and **CuP-P** benchmark catalyst (Table 2). Surface areas (SA) ranged

Table 2. Comparison of the Prepared Catalysts by N$_2$ Porosimetry

sample	SA [m^2 g^{-1}]	V_{total} [cm^3 g^{-1}]	d_{pore} [nm][a]
Aerosil 300	284	1.55	22
CuP-1	258	1.14	18
CuP-2	282	1.04	15
CuP-3	250	1.10	18
Cu-DI	245	1.45	24
CuP-Y	252	1.40	22
CuP-P	240	1.57	26

[a]Estimated by $d_{pore} = \dfrac{4 \cdot V_{total}}{SA}$.

from 250 to 282 m^2 g^{-1}, pore volumes (V_{total}) from 1.04 to 1.14 cm^3 g^{-1}, and average pore diameters (d_{pore}) from 15 to 18 nm. The N$_2$ adsorption and desorption isotherms are shown in Figure S14.

Powder X-ray diffraction analysis showed that all **Cu-phosphate/SiO$_2$** catalysts prepared from the Cu(II) phosphinate complexes and benchmark catalysts containing phosphorus (**CuP-Y**, **CuP-P**) were X-ray amorphous after calcination in the ambient atmosphere (Figure 5). On the contrary, the sample
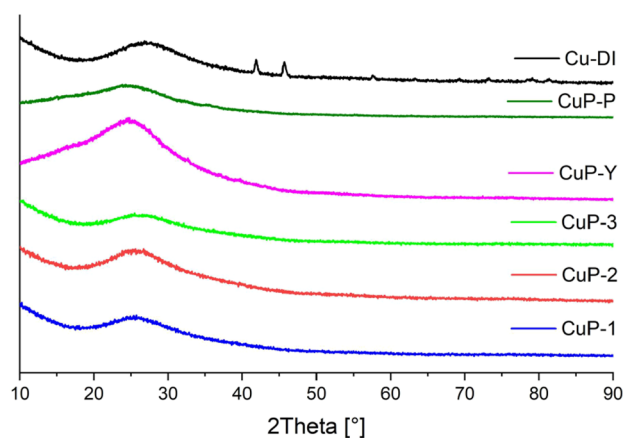
Figure 5. Comparison of the X-ray diffractograms of the fresh catalysts (calcined under an ambient atmosphere). **Cu-phosphate/SiO$_2$**, **CuP-Y**, and **CuP-P** samples are X-ray amorphous, and diffractions of CuO were observed (PDF: 00−048−1548)[121] for **Cu-DI**.

prepared by dry impregnation of copper nitrate (**Cu-DI**) exhibited diffractions corresponding to copper(II) oxide (PDF: 00−048−1548).[121] According to the Debye−Scherrer equation, the crystallite size was estimated to be 22 nm.[20]

STEM-EDS analysis of the **Cu-phosphate/SiO$_2$** samples in all cases (**CuP-1−3**) displayed small and uniform particles (Figure 6). The sample **CuP-1** prepared from the polymer precursor {Cu(SAAP)}$_n$ showed the largest nanoparticles ($\bar{A}$ = 3.4 nm; σ = 0.9 nm) of the copper phosphate phase with a broader size distribution. Thus, the polymeric nature of precursor **1** possibly leads to a slight increase in particle size in comparison with molecular ones ([Cu$_6$(BSAAP)$_6$] and [Cu$_3$(NAAP)$_3$]). It

should be noted that polymeric complex **1** can dissociate in solution into fragments with varying nuclearity (ESI-MS, see discussion above), potentially resulting in a broader size distribution of the resulting nanoparticles. Based on the graphic analysis of the STEM micrograph survey, particles in **CuP-2** prepared from [Cu$_6$(BSAAP)$_6$] exhibited the NP size of $\bar{A}$ = 2.1 nm and σ = 0.5 nm. On the other hand, the **CuP-3** catalyst prepared from [Cu$_3$(NAAP)$_3$] showed slightly larger particles ($\bar{A}$ = 2.7 nm; σ = 0.5 nm), despite the molecules of **3** (precursor for **CuP-3**) being smaller than **2**. According to STEM-EDS elemental mapping, these particles consist of Cu and P (Figure 7). Thus, it can be inferred that the particles observed in STEM-EDS micrographs present an X-ray amorphous copper phosphate phase (see below for the PXRD, TG/DSC, IR, and XPS spectroscopy study). The formation of the copper phosphate phase comes from the original application of copper phosphinates as molecular precursors.

Catalysis. Ethanol conversion over **CuP-1−3**, **CuP-Y**, **CuP-P**, and **Cu-DI** catalysts at 325 °C is shown in Figure 8. A remarkable difference in catalyst performance with time was observed between the **Cu-phosphate/SiO$_2$** catalysts and phosphorus-free **Cu-DI** (Figures 8 and 9). The sample prepared by the dry impregnation method (**Cu-DI**) achieved ethanol conversion up to 95% at the beginning of the catalytic process. The sample showed rapid deactivation during the first 5 h of the measurement (ethanol conversion dropped to ca. 70%). Afterward, the deactivation was much slower until the end of the catalytic experiment, with ethanol conversion being ca. 60% after 50 h. This behavior is in good agreement with numerous studies that have pointed out that the copper-based catalysts supported on silica often suffer from deactivation.[7,16−18,122,123]
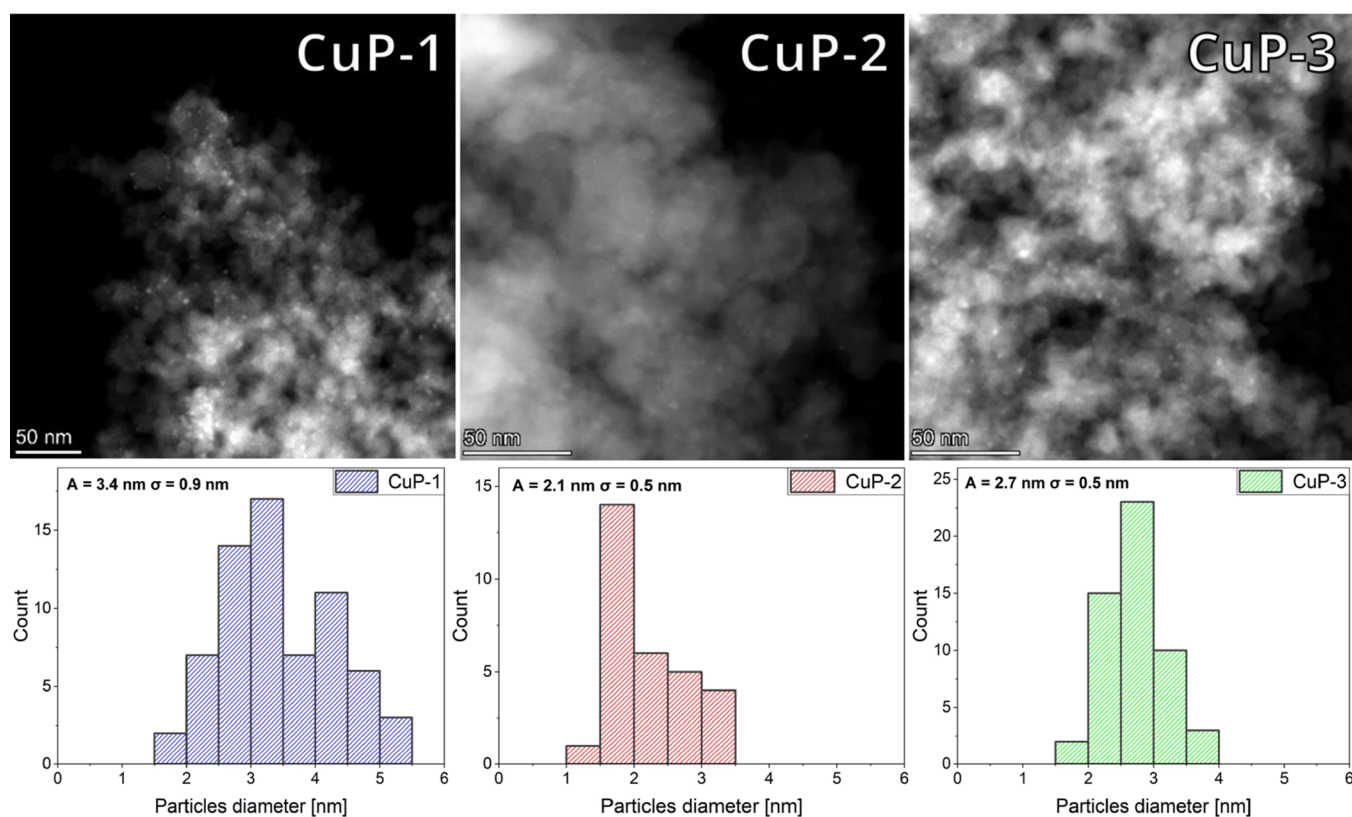

Figure 6. STEM micrographs of samples **CuP-1−3** after calcination (top) and comparison of their particle size distribution histograms (below).
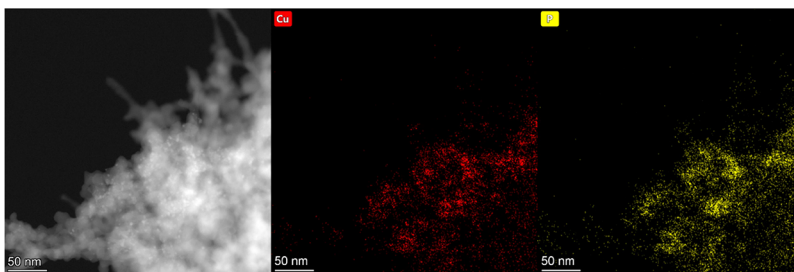
Figure 7. STEM micrograph of **CuP-1** after calcination and STEM-EDS elemental micrograph survey of copper (red) and phosphorus (yellow).
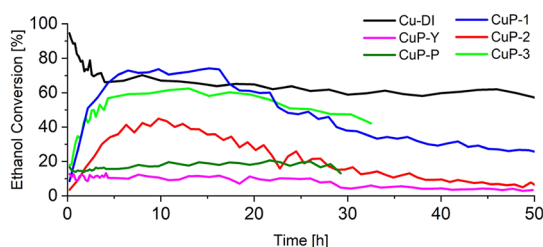

Figure 8. Evolution of ethanol conversion over time: Comparison of the benchmark catalysts (**Cu-DI**, **CuP-Y**, and **CuP-P**) with catalysts prepared from Cu(II) phosphinate complexes.
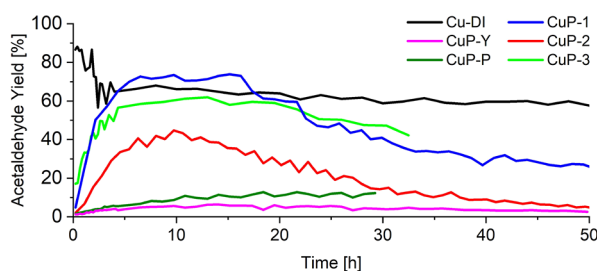

Figure 9. Acetaldehyde yield over the **Cu-phosphate/SiO₂** catalysts and comparison with the **Cu-DI**, **CuP-Y**, and **CuP-P** benchmark samples.

In contrast, the samples prepared from Cu(II) phosphinate complexes showed an initial increase in catalytic activity during the first 1.6−8 h before reaching the maximum ethanol conversion (3.3−10 h). The maximum ethanol conversion reached ca. 73% for **CuP-1**, ca. 40% for **CuP-2**, and ca. 60% for **CuP-3**, as shown in Figure 8. The ethanol conversion of **CuP-1** and **CuP-3** at the top of catalytic activity was comparable to **Cu-DI** at similar TOS (∼70%). After 6−13 h of the catalytic experiment, the course of this reaction changed, and the catalysts gradually began to deactivate, faster than **Cu-DI**. Additional catalytic experiments and analyses (ICP-OES, XPS, and STEM-EDS) were performed to better understand the catalytic behavior of the **Cu-phosphate/SiO₂** catalysts. These results are thoroughly discussed in the Changes to the Cu-Phosphate/SiO₂ Catalysts during Time-on-Stream section.

A similar behavior (i.e., an increase of the catalytic activity at the beginning and then decline) was observed in phosphorus-containing **CuP-Y** and **CuP-P** benchmark catalysts. However, the activation rate was much slower than in **Cu-phosphate/SiO₂** samples and the maximum ethanol conversion was achieved after 20−30 h. Also, the catalytic activity of **CuP-Y** and **CuP-P** catalysts was significantly lower compared to **Cu-phosphate/SiO₂**. The highest ethanol conversion was 13% for **CuP-Y** and 20% for **CuP-P**.

The acetaldehyde selectivity significantly varied among the samples. Both **Cu-phosphate/SiO₂** and phosphate-free **Cu-DI** catalysts exhibited very high selectivity to acetaldehyde (≥95% for **Cu-DI** and ≥98% for **Cu-phosphate/SiO₂**) with a carbon balance fluctuating around 95%. Therefore, the acetaldehyde yields closely followed ethanol conversion for **CuP-1−3** and **Cu-DI**. (Figures 8 and 9). On the contrary, a low selectivity to acetaldehyde was observed for phosphorus-containing benchmark catalysts (average selectivity 53% for **CuP-Y** and 43% for **CuP-P**). The ethanol dehydration to ethylene and diethyl ether was the reason for the low selectivity to acetaldehyde.

The surface Cu concentration was evaluated by XPS in all samples before and after catalytic experiments to check a possible correlation between the catalytic activity and the number of surface Cu species (Table S5). The surface Cu concentration in **CuP-1−3** is low (0.17−0.37 wt %), slightly changes with TOS, and does not correlate with the observed catalytic activity. The variations in surface Cu content are caused by the limits of XPS analysis. Cu surface content (∼0.1 at. %) is close to the detection limit,[124] and therefore quantification can be problematic. It is also possible that copper in interparticle voids is active in catalysis, but it is not "visible" via the XPS method.

Importantly, the low active phosphorus-containing benchmarks **CuP-P** and **CuP-Y** were not fully reduced to Cu^0/Cu^+ species after catalytic experiments in contrary to **CuP-1−3**: the typical peak at ∼935 eV and satellite peak at ∼944 eV for Cu^{2+} was still observed in spent samples (see Changes to the Cu-Phosphate/SiO₂ Catalysts during Time-on-Stream section). The impossibility of fully reducing copper in **CuP-P** and **CuP-Y** (and thus converting it to catalytically active Cu^0 and Cu^+ species according to literature)[125] might be connected with the phosphorus presence and will be discussed in the Changes to the Cu-Phosphate/SiO₂ Catalysts during Time-on-Stream section. Importantly, it might be one of the reasons implying a low activity of phosphorus-containing benchmark catalysts. Another reason for the low catalytic activity of **CuP-Y** and **CuP-P** might be a significant sintering of Cu particles. XRD showed intense diffractions of metallic Cu after catalytic experiments (while samples were fully XRD amorphous before catalysis; see Changes to the Cu-Phosphate/SiO₂ Catalysts during Time-on-Stream section). In agreement, STEM-EDS analysis displayed the presence of sintered particles after catalytic tests for both **CuP-Y** and **CuP-P** (∼100−500 nm; Figures S15 and S16).

The catalytic activity of the **Cu-phosphate/SiO₂** samples seemingly displayed a size dependence. Surprisingly, the most active catalyst was **CuP-1** possessing the largest particles ($\bar{A} = 3.4$ nm; $\sigma = 0.9$ nm), while the least active was **CuP-2** with the smallest particles ($\bar{A} = 2.1$ nm; $\sigma = 0.5$ nm). The particle size distribution was narrow in all three **Cu-phosphate/SiO₂**

Table 3. Comparison of Acetaldehyde Productivity at 325 °C of Cu-phosphate/SiO₂ Catalyst CuP-1 (at the Maximum Activity) with the Data Presented in the Literature (no Phosphorus in the Referenced Materials)

sample	Cu [wt %]	WHSV [h⁻¹]	T [°C]	conversion [%]	acetaldehyde selectivity [%]	acetaldehyde productivity [g g⁻¹ h⁻¹]
CuP-1[This work]	1.79	2.37	325	73	≥98	1.70
Cu/SiO₂[123]	25	2.37	300	75	94	1.67
Cu/SiO₂-AE[16]	2.7	3.16	300	98	≥99	3.07
Cu/SiO₂[20]	2.42	4.73	325	50	95	2.24
Cu/β Zeolite[17]	5	1	325	91	79	0.72

Table 4. ICP-OES Analysis of CuP-1 at the Different Stages of the Catalyst Life

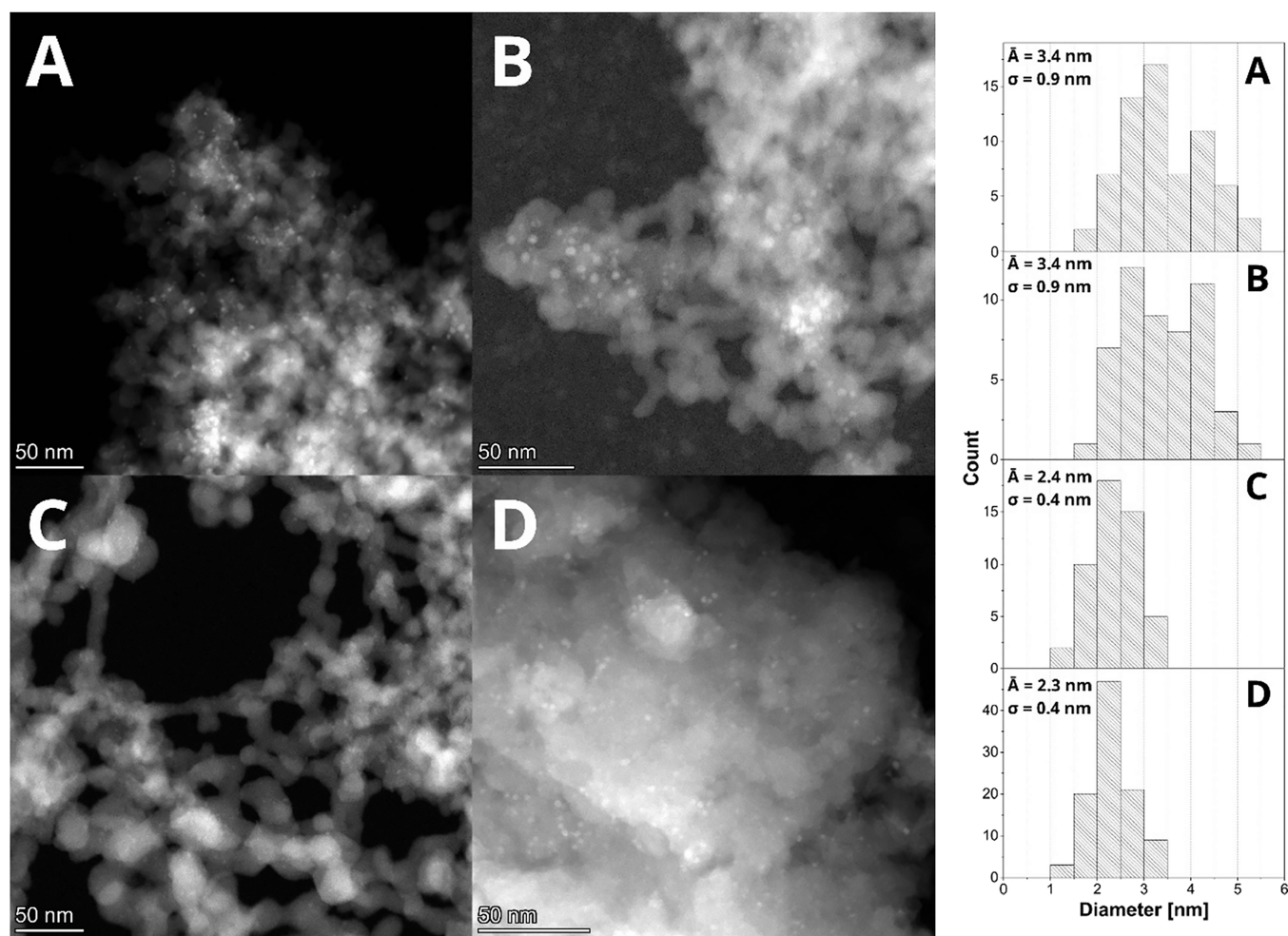| catalyst	sample	Cu loading [wt %]	P loading [wt %]	Cu:P mol ratio
	Calcined	1.79	0.93	0.93
	H₂ treated	1.75	0.92	0.93
CuP-1	At the top of catalytic activity	1.77	0.66	1.3
	Spent catalyst	1.83	0.47	1.9
CuP-Y	Spent catalyst	2.83	0.97	1.4
CuP-P	Spent catalyst	1.68	0.65	1.3

Figure 10. STEM micrographs of catalyst **CuP-1** after calcination (A), after H₂ treatment (B), at the point of the highest catalytic activity (C), and after the whole catalytic cycle (D).

catalysts and probably did not play a crucial role in catalysts performance. Also, the surface areas of the **Cu-phosphate/SiO₂** samples were similar, in the range of 250−282 m² g⁻¹, and probably did not significantly affect catalytic activity. Finally, sample **CuP-2** exhibited the highest copper loading (2.33 wt %), but it displayed the lowest catalytic activity compared to **CuP-1**

and **CuP-3,** with copper loading of 1.79 and 1.75 wt %, respectively.

Notably, the particle size was controlled by the Cu phosphinate complex used in the catalyst preparation, and thus, the precursor choice influenced the catalytic activity of the final material. The trend in catalytic activity seems to disagree

with the reports describing ethanol dehydrogenation over Cu NPs, where the smaller particles usually provide higher catalytic performance.[126] However, a thorough characterization is needed to understand better the catalytic properties of **Cu-phosphate/SiO₂** materials (see the Changes to the Cu-Phosphate/SiO₂ Catalysts during Time-on-Stream section).

Table 3 shows a comparison of previously reported catalysts and the most active newly developed **Cu-phosphate/SiO₂** catalyst **CuP-1** from this study presented at its maximum catalytic activity. **CuP-1** shows promising activity compared to other Cu-based catalysts. Despite the relatively low Cu loading of 1.79 wt %, **CuP-1** can achieve high acetaldehyde productivity with high selectivity. However, its stability needs further improvement.

Changes to the Cu-Phosphate/SiO₂ Catalysts during Time-on-Stream. Additional analyses were performed to understand the peculiar catalytic performance of the **Cu-phosphate/SiO₂** samples. The Cu:P ratio was ex-situ analyzed by ICP-OES analysis for **CuP-1** at different stages of the catalyst life: (i) calcined in ambient atmosphere, (ii) after H₂ treatment, (iii) at the maximum of ethanol conversion (i.e., after 7 h of TOS), and (iv) at the end of the catalytic experiment (after more than 50 h of TOS; Table 4). It can be seen that the Cu:P ratio did not change after H₂ treatment in comparison to the fresh calcined sample; in both cases, the ratio stayed close to 1 according to ICP-OES. During the ethanol dehydrogenation process, the amount of phosphorus steadily declined; the Cu:P ratio increased to 1.3 for the sample at the top of catalytic activity and to 1.9 at the end of the catalytic test (Table 4). Interestingly, the decrease in total phosphorus content by ICP-OES was confirmed also for phosphorus-containing benchmark catalysts **CuP-Y** and **CuP-P**. However, the phosphorus decline in sample **CuP-Y** took place to a lesser extent in comparison to **CuP-1**.

To investigate the observed phosphorus leaching over time-on-stream (TOS) in more detail, a new catalyst was prepared using complex **3** with approximately 10-fold Cu content (**CuP-3-TEP**). Subsequently, an additional catalytic experiment was conducted, and the products were collected in an ice-cooled trap (for details, see Supporting Information). The volatile compounds were then evaporated using a rotary evaporator, and the residue was analyzed by applying ¹H and ³¹P {¹H} NMR in C₆D₆ (Figure S17). The NMR spectra revealed the presence of triethyl phosphate (TEP) as the only phosphorus-containing compound. Thus, the ethanol reacts with the phosphates and converts them to TEP. The molecules of TEP are then eluted in the gas stream, and the phosphorus content in the **Cu-phosphate/SiO₂** catalysts steadily declines with TOS.

Nanoparticle sizes at the different stages of the **CuP-1** catalyst lifetime were monitored by ex-situ STEM analyses (Figure 10). Particles in the sample after H₂ treatment ($\bar{A}$ = 3.4 nm; σ = 0.9) were similar compared to the fresh catalyst, agreeing with no dramatic changes (Figure 10A,B). The increase in the catalyst activity was followed by a significant nanoparticle size decrease ($\bar{A}$ = 2.4 nm; σ = 0.5 nm) (**CuP-1** at the maximum catalytic activity; Figure 10C). STEM characterization of the spent catalyst (Figure 10D) revealed a continuous decrease in the nanoparticle size and particle size distribution.

The **Cu-phosphate/SiO₂** catalysts remained X-ray amorphous after the whole catalytic cycle (Figure 11). In contrast, the **Cu-DI**, **CuP-Y**, and **CuP-P** were reduced to metallic copper (PDF: 00−004−0836)[127] after the catalytic reaction. Moreover, as we reported recently, **Cu-DI** was reduced to metallic copper after H₂ treatment. Crystallite sizes estimated by the Debye–
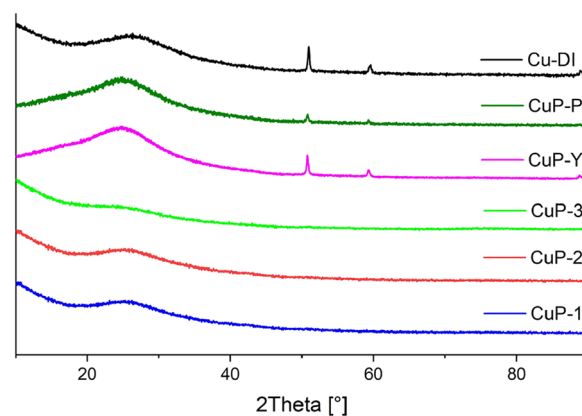

Figure 11. XRD diffraction patterns of spent catalysts; **Cu-phosphate/SiO₂** samples remained amorphous, and diffractions of metallic copper were observed (PDF: 00−004−0836)[127] for **CuP-Y**, **CuP-P**, and **Cu-DI**.

Scherrer equation for **Cu-DI** after both H₂ treatment and the whole catalytic cycle remained similar (ca. 22 nm).[20]

XPS spectra were recorded at different stages of the **CuP-1** catalyst lifetime. Both fresh calcined and H₂-treated catalysts unambiguously contain Cu²⁺ species represented by a peak at 934.3 eV[128] and a satellite peak at ∼944 eV typical for Cu²⁺ species[125] (Figure 12A,B). No evident changes were observed during the hydrogen treatment step (1 h at 400 °C). The reduction of Cu²⁺ species was observed at the maximum catalytic activity (Figure 12C). Cu²⁺ species were reduced entirely in the spent catalyst to Cu⁰/Cu⁺ (peak at 932.8 eV). Unfortunately, Cu⁰ and Cu⁺ cannot be distinguished using the Cu 2p peak[129] (Figure 12D), and the surface copper concentration is too low to observe Cu LMM signal (Auger electrons).[20]

The surface elemental composition for the different stages of catalyst lifetime, derived from XPS analyses, is presented in Table 5. The copper mass fraction increased according to XPS in the sample at the maximum catalytic activity (0.83 wt %) and then decreased for the spent catalyst (0.24 wt %). The amount of phosphorus on the surface of the spent catalyst significantly declined (Table 5). The surface phosphorus content decrease was also observed for **CuP-2**, **CuP-3**, and **CuP-P** when comparing fresh and spent catalysts (Table S5) and is obviously connected to the phosphorus leaching (confirmed by ICP-OES analysis and NMR spectroscopy).

Figure 13 displays Cu 2p XPS spectra of **Cu-phosphate/SiO₂** samples (**CuP-1**, **CuP-2**, and **CuP-3**) in comparison with all benchmarks (**CuP-Y**, **CuP-P**, and **Cu-DI**); spectra of both fresh (calcined) and spent catalysts are shown. The presence of Cu²⁺ is detected in all calcined samples. The typical peak at ∼935 eV and satellite peak at ∼944 eV confirmed the presence of oxidized copper.[128] The surface copper in **Cu-phosphate/SiO₂** samples was virtually reduced according to XPS after catalytic experiments, analogously to **Cu-DI**: the satellite peak at ∼944 eV diminished. An intense peak at ∼933 eV represents Cu⁰/Cu⁺ species which cannot be distinguished from each other.[129] On the contrary, the **CuP-Y** and **CuP-P** benchmark samples after TOS still presented a clearly observable satellite peak confirming the presence of some oxidized Cu²⁺ species.

C 1s, O 1s, P 2p, and Si 2p XPS spectra of **Cu-phosphate/SiO₂** samples (**CuP-1**, **CuP-2**, and **CuP-3**) and all benchmarks (**CuP-Y**, **CuP-P**, and **Cu-DI**) are presented in Figure S18 (fresh and calcined) and Figure S19 (spent). The C 1s spectra show an
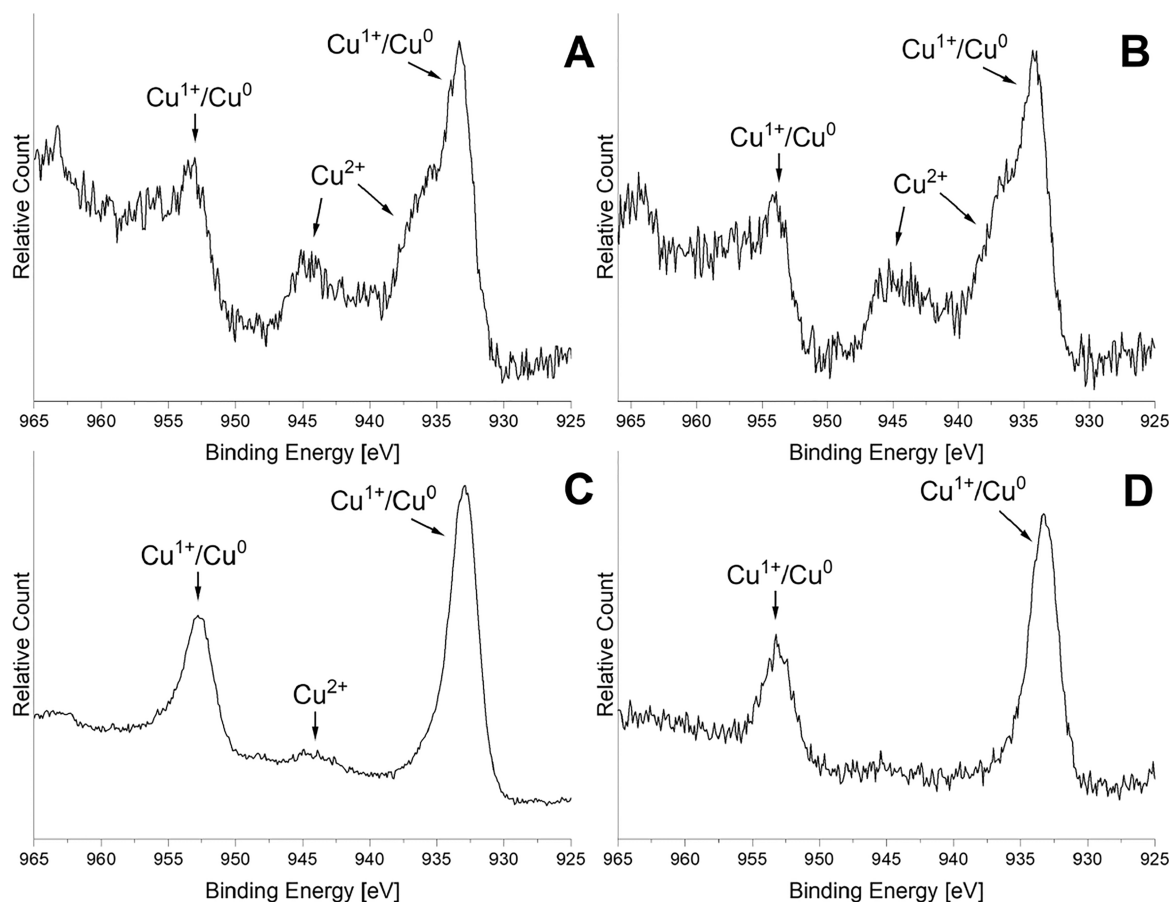
Figure 12. High-resolution XPS spectra (Cu 2p) recorded for catalyst **CuP-1** after calcination (A), after H_2 treatment (B), at the point of the highest catalytic activity (C), and after the entire catalytic cycle (D).

Table 5. XPS Analysis of CuP-1 at the Different Stages of the Catalyst Lifetime

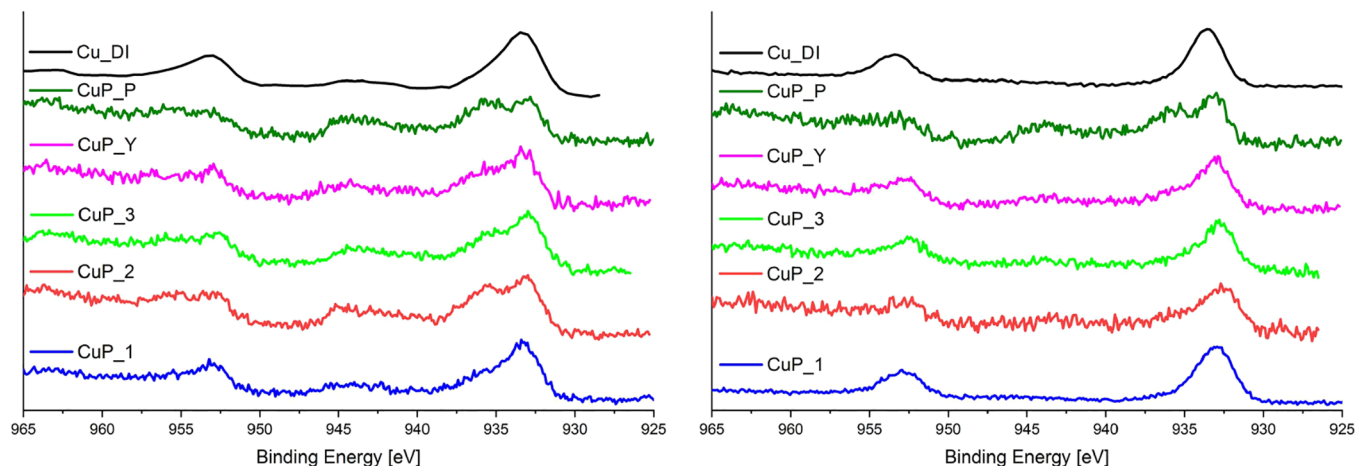| sample	Cu conc. [wt %]	P conc. [wt %]	Cu conc. [mol %]	P conc. [mol %]	Cu:P mol ratio
Calcined	0.21	0.34	0.07	0.23	0.30
H_2 treated	0.31	0.45	0.10	0.30	0.33
Top activity	0.83	0.50	0.27	0.33	0.83
Spent catalyst	0.24	0.05	0.07	0.03	2.3

Figure 13. High-resolution XPS spectra (Cu 2p) recorded for all fresh calcined catalysts (left) and after TOS (right).

expected presence of adventitious carbon, O 1s spectra present mostly oxygen in silica,[130] binding energies observed in P 2p spectra agree well with the presence of phosphate species,[131] and Si 2p spectra corroborate the nature of samples based on silica.[132,133] No changes to the chemical or oxidation state were observed upon catalytic reaction, only phosphorus content

decreased, as already discussed, and C content increased, probably due to the coke formation (see discussion below; Table S5).

Based on the results of XRD, ICP-OES, STEM-EDS, and XPS analyses described above, we propose a hypothesis regarding the possible activation and deactivation mechanisms in the **Cu-phosphate/SiO$_2$** catalysts. First, Cu^{2+} species in the **Cu-phosphate/SiO$_2$** catalysts and phosphorus-containing benchmark samples were not completely reduced (XPS) after H$_2$ treatment and, therefore, exhibited a low activity. Cu reduction before ethanol dehydrogenation is a common pretreatment step and leads to catalyst activation.[16,134] A possible explanation for the ineffective H$_2$ treatment of the **Cu-phosphate/SiO$_2$** catalysts could be the presence of the Cu-phosphate phase with intimate Cu and P mixing, as suggested by STEM-EDS analyses (see Synthesis and Characterization of Cu-Phosphate/SiO2 Catalysts section). Metal phosphates are generally much more resistant to reduction than corresponding metal oxides.[135]

H$_2$-TPR analyses support the first part of our hypothesis (Figure 14). Obviously, only the **Cu-DI** benchmark catalyst was
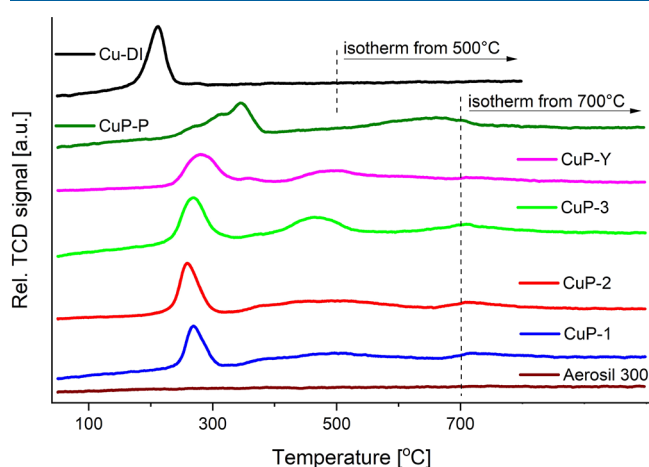
Figure 14. H$_2$-TPR analysis of **Cu-phosphate/SiO$_2$** and the benchmark catalysts. The isothermal part of the measurements of the TCD signal was conducted at 700 °C for all phosphorus-containing samples and at 500 °C for the **Cu-DI** sample.

fully reduced up to 400 °C, while **Cu-phosphate/SiO$_2$** catalysts were only partly reduced at this temperature. As a result, not all Cu species could participate in the catalytic reaction. The maximum of the main peak was observed at a temperature of 211 °C for the **Cu-DI** benchmark catalyst. This peak was shifted to higher temperatures in the case of **Cu-phosphate/SiO$_2$** catalysts (Figure 14; Table S6), similar to other Cu/P-SiO$_2$ catalysts.[136] Also, other peaks were found at higher temperatures (>400 °C; Figure 14; Table S6), and their shapes and positions were different for each individual sample. In the case of both phosphorus-containing benchmark catalysts (**CuP-Y** and **CuP-P**), the first main peak was broader; moreover, the most different shape of this peak was observed for the **CuP-P** benchmark catalyst (Figure 14; Table S6). The Cu concentrations calculated from the H$_2$ consumptions during the H$_2$-TPR analyses range from 1.7 to 2.6 wt % (Table S6) and are thus comparable to the Cu loadings estimated by ICP-OES analyses (Table 1).

The activated **CuP-1** catalyst (i.e., at the top of catalytic activity) exhibited a higher Cu:P ratio both in bulk and the surface layer (ICP-OES, Table 4; XPS, Table 5), smaller particle

size (STEM; Figure 10), and a higher Cu surface content (XPS; Table 5) than the nonactive (freshly calcined) sample. Also, the Cu^{2+} species were mostly reduced to Cu^0/Cu$^+$ during time-on-stream (TOS) according to XPS analyses (Figure 12). Apparently, phosphorus leaching from the **Cu-phosphate/SiO$_2$** catalysts during TOS enabled Cu reduction. These processes could be simultaneous. Ethanol and H$_2$ (originating in ethanol dehydrogenation) can be put forward as possible reducing agents. As already discussed, Cu reduction is necessary for its activation in the ethanol dehydrogenation reaction.[137] The decrease in particle size and increase in the Cu surface content may also have a beneficial effect on the catalytic activity as well. It correlates well with the observed increase in catalytic activity during the first 1.6−8.3 h of catalytic reaction in **CuP-1−3**.

Finally, the **Cu-phosphate/SiO$_2$** samples started to deactivate after a period of high catalytic activity. Two deactivation mechanisms are primarily discussed in the literature: sintering of Cu particles and coking.[16−18,122] Cu sintering has not been observed in our case: the samples remained XRD amorphous (Figure 11), and no large particles were observed by STEM-EDS (Figure 10). Therefore, we focused our attention on possible coking and analyzed the carbon content by XPS. The XPS analysis of the catalyst surface suggests that there is no significant coking, as the carbon content at the maximum of catalytic activity (3.49 wt %) is virtually the same as in that of the spent catalyst after 50 h of TOS (3.51 wt %), as shown in Table 6. The

Table 6. Study of Coking by XPS Analysis of CuP-1 at the Different Stages of Catalyst Life

sample	carbon content [wt %]
Calcined	2.24
H$_2$ treated	3.74
Top activity	3.49
Spent catalyst	3.51

other spent phosphorus-containing catalysts exhibited a similar surface C content (2.93−3.56 wt %), while **Cu-DI** showed a somewhat higher surface C concentration (4.33 wt %; Table S5). The presence of coking is usually clearly observed after such extensive TOS.[20] Notably, our findings agree with previous studies, which suggest that adding phosphorus to zeolite catalysts can prevent coking.[105,106] Based on the results, an alternative deactivation mechanism can be suggested. The STEM-EDS micrographs of spent catalyst demonstrate a significant decrease in particle size (from 3.4 to 2.3 nm on average; ~32%). At the same time, the Cu surface content significantly decreased (XPS; Table 5). Therefore, we hypothesize that Cu might diffuse into the SiO$_2$ support and become inaccessible and, in turn, inactive. The stable Cu content in **CuP-1** at the different stages of catalyst lifetime (~1.8 wt %; ICP-OES; Table 4) excludes the catalyst deactivation by the copper leaching. The Cu diffusion in silica-based catalysts has already been observed at the temperatures below T_{Tamman}.[21]

■ CONCLUSIONS

In this study, three new Cu-phosphate-based catalysts were prepared using three newly synthesized well-soluble Cu(II) phosphinate complexes of different nuclearities: a polymeric (**1**), a hexanuclear (**2**), and a trinuclear (**3**) complex. The structures of complexes **1−3** were fully characterized and described in detail. Impregnation of the molecular precursors

1−3 on silica provided **Cu-phosphate/SiO₂** materials with homogeneously dispersed nanoparticles (2.1–3.4 nm) and narrow particle size distribution. The polymeric complex (**1**) provided larger particles with a broader distribution than the hexanuclar (**2**) and trinuclear (**3**) complexes. The particles consisted of both Cu and P according to STEM-EDS analyses. The **Cu-phosphate/SiO₂** materials were evaluated as catalysts in nonoxidative ethanol dehydrogenation and compared with the conventional benchmark Cu-based catalyst prepared by dry impregnation (**Cu-DI**), as well as Cu-based catalysts containing phosphorus (**CuP-Y** and **CuP-P**). Our results demonstrate a distinctively different catalytic behavior of the **Cu-phosphate/SiO₂** materials compared to the conventional Cu-based catalysts (**Cu-DI**). These materials also exhibited significantly higher activity when compared to those containing phosphorus (**CuP-Y** and **CuP-P**), but only comparable activity and lower stability in comparison to the phosphorus-free **Cu-DI** benchmark. By investigating the catalyst (**CuP-1**) life cycle, we uncovered the changes in the material influencing the catalytic properties. The increase of catalytic activity during TOS was related to the decrease of phosphorus content in both bulk and the surface layer and to the copper reduction. The maximum ethanol conversion was reached during 1.6−8 h of TOS, namely, ca. 73% for **CuP-1**, ca. 40% for **CuP-2**, and ca. 60% for **CuP-3**, while selectivity to acetaldehyde remained over 98% at WHSV = 2.37 h⁻¹ for all catalysts. However, a steady decrease in catalytic activity was observed after the catalysts reached their maximum performance. The deactivation process was suggested to be related to Cu diffusion: the surface Cu concentration decreased together with the average particle size. The comparison of stability with TOS suggests that different strategies need to be explored to improve the long-term stability of Cu-based catalysts. Overall, our study demonstrates a new approach to P-doped Cu-based catalysts with intimate Cu and P mixing and sheds light on their peculiar behavior in nonoxidative ethanol dehydrogenation.

ASSOCIATED CONTENT

Ⓢ Supporting Information

The Supporting Information is available free of charge at https://pubs.acs.org/doi/10.1021/acs.inorgchem.3c01678.

> Synthesis of the ligands and their characterization (ICP-OES, IR, and NMR); synthesis of copper phosphinate complexes and their characterization (ICP-OES, IR, and ESI-MS), crystallographic parameters, selected bond lengths, CShM analysis of the polyhedra of the prepared complexes, details of catalysts preparation (masses of copper phosphinates and support), XPS surface measurement of Cu, P, and C, and H₂-TPR results, ESI-MS, TG, PXRD, IR analyses of the prepared and calcined complexes, and adsorption isotherms of prepared catalysts and support; STEM-EDS analysis of benchmark **CuP-Y** and **CuP-P** samples after catalysis, and NMR spectra of obtained TEP, and XPS surface measurement of C, O, P, and Si on freshly calcined and spent catalysts (PDF)

Accession Codes

CCDC 2252549−2252551 contain the supplementary crystallographic data for this paper. These data can be obtained free of charge via www.ccdc.cam.ac.uk/data_request/cif, or by emailing data_request@ccdc.cam.ac.uk, or by contacting The Cambridge Crystallographic Data Centre, 12 Union Road, Cambridge CB2 1EZ, UK; fax: +44 1223 336033.

AUTHOR INFORMATION

Corresponding Author

Ales Styskalik − *Department of Chemistry, Faculty of Science, Masaryk University, CZ-61137 Brno, Czech Republic;* ⓞ orcid.org/0000-0002-9998-6978; Phone: +420549498702; Email: styskalik@chemi.muni.cz

Authors

Tomas Pokorny − *Department of Chemistry, Faculty of Science, Masaryk University, CZ-61137 Brno, Czech Republic;* ⓞ orcid.org/0000-0002-6780-4738

Iaroslav Doroshenko − *Department of Chemistry, Faculty of Science, Masaryk University, CZ-61137 Brno, Czech Republic;* ⓞ orcid.org/0000-0002-5279-5517

Petr Machac − *Department of Chemistry, Faculty of Science, Masaryk University, CZ-61137 Brno, Czech Republic*

Lucie Simonikova − *Department of Chemistry, Faculty of Science, Masaryk University, CZ-61137 Brno, Czech Republic*

Miroslava Bittova − *Department of Chemistry, Faculty of Science, Masaryk University, CZ-61137 Brno, Czech Republic*

Zdenek Moravec − *Department of Chemistry, Faculty of Science, Masaryk University, CZ-61137 Brno, Czech Republic*

Katerina Karaskova − *Institute of Environmental Technology, CEET, VSB-TUO, CZ-70800 Ostrava, Czech Republic*

David Skoda − *Centre of Polymer Systems, Tomas Bata University in Zlin, CZ-76001 Zlin, Czech Republic;* ⓞ orcid.org/0000-0002-3787-1956

Jiri Pinkas − *Department of Chemistry, Faculty of Science, Masaryk University, CZ-61137 Brno, Czech Republic;* ⓞ orcid.org/0000-0002-6234-850X

Complete contact information is available at:
https://pubs.acs.org/10.1021/acs.inorgchem.3c01678

Author Contributions

‖T.P. and I.D. contributed equally to this work and should be considered cofirst authors.

Author Contributions

T.P.: Investigation, writing—original draft, and visualization; I.D.: investigation, writing—original draft, and visualization; P.M.: investigation and writing − review and editing; L.S.: investigation and writing − review and editing; M.B.: investigation and writing − review and editing; Z.M.: investigation and writing − review and editing; K.K.: investigation and writing − review and editing; D.S.: investigation and writing − review and editing; J.P.: conceptualization, methodology, writing − review and editing, supervision, and funding acquisition; A.S.: conceptualization, methodology, writing − review and editing, supervision, and funding acquisition.

Notes

The authors declare no competing financial interest.

■ ABBREVIATIONS

CShM, continuous shape measures; DI, dry impregnation; EDS, energy dispersive spectroscopy; FID, flame ionization detector; IR, infrared spectroscopy; FTIR, Fourier transformation infrared spectroscopy; ATR, attenuated total reflectance; ICP-OES, inductively coupled plasma optical emission spectroscopy; STEM-EDS, scanning transmission electron microscopy with energy dispersive spectroscopy; TG, thermogravimetry; TOS, time-on-stream; XPS, X-ray photoelectron spectroscopy

■ REFERENCES

(1) Graedel, T. Green Chemistry in an Industrial Ecology Context. *Green Chem.* **1999**, *1* (5), 126−128.

(2) Clark, J. H. Green Chemistry: Challenges and Opportunities. *Green Chem.* **1999**, *1* (1), 1−8.

(3) Liu, P.; Hensen, E. J. M. Highly Efficient and Robust Au/MgCuCr$_2$O$_4$ Catalyst for Gas-Phase Oxidation of Ethanol to Acetaldehyde. *J. Am. Chem. Soc.* **2013**, *135* (38), 14032−14035.

(4) Takei, T.; Iguchi, N.; Haruta, M. Synthesis of Acetoaldehyde, Acetic Acid, and Others by the Dehydrogenation and Oxidation of Ethanol. *Catal. Surv. from Asia* **2011**, *15* (2), 80−88.

(5) Patel, A. C.; Li, S.; Wang, C.; Zhang, W.; Wei, Y. Electrospinning of Porous Silica Nanofibers Containing Silver Nanoparticles for Catalytic Applications. *Chem. Mater.* **2007**, *19* (6), 1231−1238.

(6) Cespi, D.; Passarini, F.; Vassura, I.; Cavani, F. Butadiene from Biomass, a Life Cycle Perspective to Address Sustainability in the Chemical Industry. *Green Chem.* **2016**, *18* (6), 1625−1638.

(7) Pomalaza, G.; Arango Ponton, P.; Capron, M.; Dumeignil, F. Ethanol-to-Butadiene: The Reaction and Its Catalysts. *Catal. Sci. Technol.* **2020**, *10* (15), 4860−4911.

(8) Shylesh, S.; Gokhale, A. A.; Scown, C. D.; Kim, D.; Ho, C. R.; Bell, A. T. From Sugars to Wheels: The Conversion of Ethanol to 1,3-Butadiene over Metal-Promoted Magnesia-Silicate Catalysts. *ChemSusChem* **2016**, *9* (12), 1462−1472.

(9) Jira, R. Acetaldehyde from Ethylene-A Retrospective on the Discovery of the Wacker Process. *Angew. Chemie Int. Ed.* **2009**, *48* (48), 9034−9037.

(10) Keith, J. A.; Nielsen, R. J.; Oxgaard, J.; Goddard, W. A. Unraveling the Wacker Oxidation Mechanisms. *J. Am. Chem. Soc.* **2007**, *129* (41), 12342−12343.

(11) Lebedev Process. In *Comprehensive Organic Name Reactions and Reagents*; John Wiley & Sons, Inc.: Hoboken, NJ, USA, 2010.

(12) Angelici, C.; Velthoen, M. E. Z.; Weckhuysen, B. M.; Bruijnincx, P. C. A. Influence of Acid−Base Properties on the Lebedev Ethanol-to-Butadiene Process Catalyzed by SiO$_2$−MgO Materials. *Catal. Sci. Technol.* **2015**, *5* (5), 2869−2879.

(13) Segawa, A.; Nakashima, A.; Nojima, R.; Yoshida, N.; Okamoto, M. Acetaldehyde Production from Ethanol by Eco-Friendly Non-Chromium Catalysts Consisting of Copper and Calcium Silicate. *Ind. Eng. Chem. Res.* **2018**, *57* (35), 11852−11857.

(14) Freitas, I. C.; Damyanova, S.; Oliveira, D. C.; Marques, C. M. P.; Bueno, J. M. C. Effect of Cu Content on the Surface and Catalytic Properties of Cu/ZrO2 Catalyst for Ethanol Dehydrogenation. *J. Mol. Catal. A Chem.* **2014**, *381*, 26−37.

(15) Chang, F. W.; Yang, H. C.; Roselin, L. S.; Kuo, W. Y. Ethanol Dehydrogenation over Copper Catalysts on Rice Husk Ash Prepared by Ion Exchange. *Appl. Catal. A Gen.* **2006**, *304* (1−2), 30−39.

(16) Zhang, H.; Tan, H. R.; Jaenicke, S.; Chuah, G. K. Highly Efficient and Robust Cu Catalyst for Non-Oxidative Dehydrogenation of Ethanol to Acetaldehyde and Hydrogen. *J. Catal.* **2020**, *389*, 19−28.

(17) Yu, D.; Dai, W.; Wu, G.; Guan, N.; Li, L. Stabilizing Copper Species Using Zeolite for Ethanol Catalytic Dehydrogenation to Acetaldehyde. *Chin. J. Catal.* **2019**, *40* (9), 1375−1384.

(18) Ob-eye, J.; Praserthdam, P.; Jongsomjit, B. Dehydrogenation of Ethanol to Acetaldehyde over Different Metals Supported on Carbon Catalysts. *Catalysts* **2019**, *9* (1), 66.

(19) Chang, F. W.; Kuo, W. Y.; Lee, K. C. Dehydrogenation of Ethanol over Copper Catalysts on Rice Husk Ash Prepared by Incipient Wetness Impregnation. *Appl. Catal. A Gen.* **2003**, *246* (2), 253−264.

(20) Pokorny, T.; Vykoukal, V.; Machac, P.; Moravec, Z.; Scotti, N.; Roupcova, P.; Karaskova, K.; Styskalik, A. Ethanol Dehydrogenation over Copper-Silica Catalysts: From Sub-Nanometer Clusters to 15 Nm Large Particles. *ACS Sustain. Chem. Eng.* **2023**, *11* (30), 10980−10992.

(21) Pampararo, G.; Garbarino, G.; Riani, P.; Vykoukal, V.; Busca, G.; Debecker, D. P. Ethanol Dehydrogenation to Acetaldehyde with Mesoporous Cu-SiO$_2$ Catalysts Prepared by Aerosol-Assisted Sol−Gel. *Chem. Eng. J.* **2023**, *465*, No. 142715.

(22) Tu, Y. J.; Chen, Y. W. Effects of Alkali Metal Oxide Additives on Cu/SiO$_2$ Catalyst in the Dehydrogenation of Ethanol. *Ind. Eng. Chem. Res.* **2001**, *40* (25), 5889−5893.

(23) Coles, M. P.; Lugmair, C. G.; Terry, K. W.; Tilley, T. D. Titania-Silica Materials from the Molecular Precursor Ti[OSi(O^{t}Bu)$_3$]$_4$: Selective Epoxidation Catalysts. *Chem. Mater.* **2000**, *12* (1), 122−131.

(24) Jarupatrakorn, J.; Tilley, T. D. Silica-Supported, Single-Site Titanium Catalysts for Olefin Epoxidation. A Molecular Precursor Strategy for Control of Catalyst Structure. *J. Am. Chem. Soc.* **2002**, *124* (28), 8380−8388.

(25) Singh, A.; Chang, S. L. Y.; Hocking, R. K.; Bach, U.; Spiccia, L. Highly Active Nickel Oxide Water Oxidation Catalysts Deposited from Molecular Complexes. *Energy Environ. Sci.* **2013**, *6* (2), 579−586.

(26) Khemthong, P.; Daorattanachai, P.; Laosiripojana, N.; Faungnawakij, K. Copper Phosphate Nanostructures Catalyze Dehydration of Fructose to 5-Hydroxymethylfufural. *Catal. Commun.* **2012**, *29*, 96−100.

(27) Zhong, G.; Bai, J.; Duchesne, P. N.; McDonald, M. J.; Li, Q.; Hou, X.; Tang, J. A.; Wang, Y.; Zhao, W.; Gong, Z.; Zhang, P.; Fu, R.; Yang, Y. Copper Phosphate as a Cathode Material for Rechargeable Li Batteries and Its Electrochemical Reaction Mechanism. *Chem. Mater.* **2015**, *27* (16), 5736−5744.

(28) Soták, T.; Hronec, M.; Gál, M.; Dobročka, E.; Škriniarová, J. Aqueous-Phase Oxidation of Furfural to Maleic Acid Catalyzed by Copper Phosphate Catalysts. *Catal. Lett.* **2017**, *147* (11), 2714−2723.

(29) Xie, W.-Y.; Song, F.; Wang, X.-L.; Wang, Y.-Z. Development of Copper Phosphate Nanoflowers on Soy Protein toward a Superhydrophobic and Self-Cleaning Film. *ACS Sustain. Chem. Eng.* **2017**, *5* (1), 869−875.

(30) Luo, Y. K.; Song, F.; Wang, X. L.; Wang, Y. Z. Pure Copper Phosphate Nanostructures with Controlled Growth: A Versatile Support for Enzyme Immobilization. *CrystEngComm* **2017**, *19* (22), 2996−3002.

(31) Wu, H.; Song, J.; Xie, C.; Hu, Y.; Liu, S.; Han, B. Preparation of Copper Phosphate from Naturally Occurring Phytic Acid as an Advanced Catalyst for Oxidation of Aromatic Benzyl Compounds. *ACS Sustain. Chem. Eng.* **2018**, *6* (11), 13670−13675.

(32) Nag, R.; Rao, C. P. Development and Demonstration of Functionalized Inorganic−Organic Hybrid Copper Phosphate Nano-

flowers for Mimicking the Oxidative Reactions of Metalloenzymes by Working as a Nanozyme. *J. Mater. Chem. B* **2021**, *9* (16), 3523−3532.

(33) Rahmani, F.; Ghadi, A.; Doustkhah, E.; Khaksar, S. In Situ Formation of Copper Phosphate on Hydroxyapatite for Wastewater Treatment. *Nanomaterials* **2022**, *12* (15), 2650.

(34) Prapakaran, T.; Sathish, C. I.; Yi, J.; Vinu, A.; Murugavel, R. Nuclearity Control in Molecular Copper Phosphates Derived from a Bulky Arylphosphate: Synthesis, Structural and Magnetic Studies. *Eur. J. Inorg. Chem.* **2023**, *26* (17), No. e202300071.

(35) Zhang, Y.; Clearfield, A. Synthesis, Crystal Structures, and Coordination Intercalation Behavior of Two Copper Phosphonates. *Inorg. Chem.* **1992**, *31* (13), 2821−2826.

(36) Le Bideau, J.; Payen, C.; Palvadeau, P.; Bujoli, B. Preparation Structure, and Magnetic Properties of Copper(II) Phosphonates. .Beta.-CuII(CH3PO3), an Original Three-Dimensional Structure with a Channel-Type Arrangement. *Inorg. Chem.* **1994**, *33* (22), 4885−4890.

(37) Chandrasekhar, V.; Sahoo, D.; Narayanan, R. S.; Butcher, R. J.; Lloret, F.; Pardo, E. A Hexaicosametallic Copper(II) Phosphonate. *Dalt. Trans.* **2013**, *42* (23), 8192−8196.

(38) Hermer, N.; Stock, N. The New Triazine-Based Porous Copper Phosphonate $[Cu_3(PPT)(H_2O)_3] \cdot 10H_2O$. *Dalt. Trans.* **2015**, *44* (8), 3720−3723.

(39) Ai, J.; Min, X.; Gao, C. Y.; Tian, H. R.; Dang, S.; Sun, Z. M. A Copper-Phosphonate Network as a High-Performance Heterogeneous Catalyst for the CO_2 Cycloaddition Reactions and Alcoholysis of Epoxides. *Dalt. Trans.* **2017**, *46* (20), 6756−6761.

(40) Wang, J. M.; Liu, Y. R.; Mao, X. Y.; Shi, N. N.; Zhang, X.; Wang, H. S.; Fan, Y. H.; Wang, M. Two Trinuclear CuII Complexes: Effect of Phosphonate Ligand on the Magnetic Property and Electrocatalytic Reactivity for Water Oxidation. *Chem. − Asian J.* **2019**, *14* (15), 2685−2693.

(41) Liu, B.; Liu, J. C.; Shen, Y.; Feng, J. S.; Bao, S. S.; Zheng, L. M. Polymorphic Layered Copper Phosphonates: Exfoliation and Proton Conductivity Studies. *Dalt. Trans.* **2019**, *48* (19), 6539−6545.

(42) Peeples, C. A.; Kober, D.; Schmitt, F.; Tholen, P.; Siemensmeyer, K.; Halldorson, Q.; Çoşut, B.; Gurlo, A.; Yazaydin, A. O.; Hanna, G.; Yücesan, G. A 3D Cu-Naphthalene-Phosphonate Metal−Organic Framework with Ultra-High Electrical Conductivity. *Adv. Funct. Mater.* **2021**, *31* (3), No. 2007294.

(43) Hu, Z. J.; Tsai, M. J.; Sung, H. L.; Wu, J. Y. A Three-Component Copper Phosphonate Complex as a Sensor Platform for Sensitive Cd^{2+} and Zn^{2+} Ion Detection in Water via Fluorescence Enhancement. *J. Solid State Chem.* **2021**, *299*, No. 122178.

(44) Pankhurst, J. R.; Castilla-Amorós, L.; Stoian, D. C.; Vavra, J.; Mantella, V.; Albertini, P. P.; Buonsanti, R. Copper Phosphonate Lamella Intermediates Control the Shape of Colloidal Copper Nanocrystals. *J. Am. Chem. Soc.* **2022**, *144* (27), 12261−12271.

(45) Salcedo-Abraira, P.; Serrano-Nieto, R.; Biglione, C.; Cabrero-Antonino, M.; Vilela, S. M. F.; Babaryk, A. A.; Tilve-Martínez, D.; Rodriguez-Diéguez, A.; Navalón, S.; García, H.; Horcajada, P. Two Cu-Based Phosphonate Metal−Organic Frameworks as Efficient Water-Splitting Photocatalysts. *Chem. Mater.* **2023**, *35* (11), 4211−4219.

(46) Chandrasekhar, V.; Kingsley, S. A Dodecanuclear Copper(Ii) Cage Containing Phosphonate and Pyrazole Ligands**. *Angew. Chem., Int. Ed.* **2000**, *39* (13), 2320.

(47) Yao, H.-C.; Li, Y.-Z.; Gao, S.; Song, Y.; Zheng, L.-M.; Xin, X.-Q. Copper Phosphonates with Dinuclear and Layer Structures: A Structural and Magnetic Study. *J. Solid State Chem.* **2004**, *177* (12), 4557−4563.

(48) Chandrasekhar, V.; Senapati, T.; Sañudo, E. C. Synthesis, Structure, and Magnetism of Hexanuclear Copper(II) Phosphonates. *Inorg. Chem.* **2008**, *47* (20), 9553−9560.

(49) Chandrasekhar, V.; Nagarajan, L.; Clérac, R.; Ghosh, S.; Verma, S. A Distorted Cubic Tetranuclear Copper(II) Phosphonate Cage with a Double-Four-Ring-Type Core. *Inorg. Chem.* **2008**, *47* (3), 1067−1073.

(50) Chandrasekhar, V.; Nagarajan, L. A Hexadecameric Copper(II) Phosphonate. *Dalt. Trans.* **2009**, *34*, 6712−6714.

(51) Chandrasekhar, V.; Senapati, T.; Dey, A.; Sañudo, E. C. Rational Assembly of Soluble Copper(II) Phosphonates: Synthesis, Structure and Magnetism of Molecular Tetranuclear Copper(II) Phosphonates. *Inorg. Chem.* **2011**, *50* (4), 1420−1428.

(52) Chandrasekhar, V.; Nagarajan, L.; Hossain, S.; Gopal, K.; Ghosh, S.; Verma, S. Multicomponent Assembly of Anionic and Neutral Decanuclear Copper(II) Phosphonate Cages. *Inorg. Chem.* **2012**, *51* (10), 5605−5616.

(53) Taddei, M.; Costantino, F.; Ienco, A.; Comotti, A.; Dau, P. V.; Cohen, S. M. Synthesis, Breathing, and Gas Sorption Study of the First Isoreticular Mixed-Linker Phosphonate Based Metal−Organic Frameworks. *Chem. Commun.* **2013**, *49* (13), 1315.

(54) Cini, R.; Colamarino, P.; Orioli, P. L.; Smith, L. S.; Newman, P. R.; Gillman, H. D.; Nannelli, P. Crystal Structure and Magnetic Studies of Bis(.Mu.-Dibutylphosphinato)-Copper(II). *Inorg. Chem.* **1977**, *16* (12), 3223−3226.

(55) Gillman, H. D.; Eichelberger, J. L. Inorganic Coordination Polymers. XXII. Manganese(II), Cobalt(II), Nickel(II), Copper(II), and Zinc(II) Bis[Bis(N-Phenylaminomethyl)Phosphinates]. Effects of Coordinating Side Groups. *Inorg. Chim. Acta* **1977**, *24* (C), 31−34.

(56) Oliver, K. W.; Rettig, S. J.; Thompson, R. C.; Trotter, J.; Xia, S. Crystal Structure and Magnetic Behavior of Copper(II) Dimethyl-phosphinate: A Chain Polymer Containing Triangular Trimetallic Bis(μ-Dimethylphosphinato)Copper(II) Units. *Inorg. Chem.* **1997**, *36* (11), 2465−2468.

(57) Cecconi, F.; Ghilardi, C. A.; Lorenzo Luis, P. A.; Midollini, S.; Orlandini, A.; Dakternieks, D.; Duthie, A.; Dominguez, S.; Berti, E.; Vacca, A. Complexes of the Tripodal Nitrilotrimethylenetrisphos-phonic (H_6L) and P,P′,P″-Triphenylnitrilotrimethylenetrisphosphinic ($H_3L°$) Acids with the Copper(II) Ion. Synthesis and Characterization of $[Hpy][Cu(H_3L)(H_2O)]$ and $[Cu(HL°)(Py)]_2 \cdot 2Me_2CO$. *J. Chem. Soc. Dalt. Trans.* **2001**, *2*, 211−217.

(58) Sergienko, V. S. Structural Features of 3d Metal Compounds with 1-Hydroxyethylidenediphosphonic Acid. *Crystallogr. Reports* **2001**, *46* (2), 196−206.

(59) Chiang, M. Y.-N.; Wu, J.-Y.; Zeng, W.-F.; Xu, D.-J. Bis(Di-2-Pyridylphosphinato-κ^3N,O,N')Copper(II) Dichloromethane Disolvate. *Acta Crystallogr. Sect. C Cryst. Struct. Commun.* **2003**, *59* (12), m523−m525.

(60) Kubíček, V.; Vojtíšek, P.; Rudovsky, J.; Hermann, P.; Lukeš, I. Complexes of Divalent Transition Metal Ions with Bis(Aminomethyl)-Phosphinic Acid in Aqueous Solution and in the Solid State. *Dalt. Trans.* **2003**, *20*, 3927−3938.

(61) Koga, K.; Ohtsubo, M.; Yamada, Y.; Koikawa, M.; Tokii, T. Novel Dinuclear Copper(II) Complexes with Syn-Syn and Syn-Anti Coordination Modes of Bis(μ-Phosphinato)-Bridges: Structures and Magnetic Properties. *Chem. Lett.* **2004**, *33* (12), 1606−1607.

(62) Ciattini, S.; Costantino, F.; Lorenzo-Luis, P.; Midollini, S.; Orlandini, A.; Vacca, A. Inorganic−Organic Hybrids Formed by P,P′-Diphenylmethylenediphosphinate, Pcp^{2-}, with the Cu^{2+} Ion. X-Ray Crystal Structures of $[Cu(Pcp)(H_2O)_2] \cdot H_2O$ and $[Cu(Pcp)(Bipy)(H_2O)]$. *Inorg. Chem.* **2005**, *44* (11), 4008−4016.

(63) Midollini, S.; Orlandini, A. Hydrogen Bonding in Triamine Copper(II) P,P′-Diphenylmethylenediphosphinate (Pcp^{2-}) Hybrids. Syntheses and Crystal Structures of $[Cu(Pcp)(2,2′-Dipyridylamine)(H_2O)] \cdot 2H_2O$ and $[Cu(Pcp)(2,2′: 6′,2″terpyridine)] \cdot 4H_2O$. *J. Coord. Chem.* **2006**, *59* (13), 1433−1442.

(64) Kubíček, V.; Řehoř, I.; Havlíčková, J.; Kotek, J.; Císařová, I.; Hermann, P.; Lukeš, I. Synthesis and Coordination Behavior of Symmetrical Tetraamine Phosphinic Acids. *Eur. J. Inorg. Chem.* **2007**, *2007* (24), 3881−3891.

(65) Murugavel, R.; Pothiraja, R.; Gogoi, N.; Clérac, R.; Lecren, L.; Butcher, R. J.; Nethaji, M. Synthesis, Magnetic Behaviour, and X-Ray Structures of Dinuclear Copper Complexes with Multiple Bridges. Efficient and Selective Catalysts for Polymerization of 2,6-Dimethyl-phenol. *Dalton Trans.* **2007**, *23*, 2405−2410.

(66) Oliver, K. W.; Rettig, S. J.; Thompson, R. C.; Trotter, J. Synthesis, Structure, and Properties of Poly-Bis(μ-Diethylphosphinato)Copper-(II). *Can. J. Chem.* **1982**, *60* (15), 2017−2022.

(67) Tircsó, G.; Bényei, A.; Király, R.; Lázár, I.; Pál, R.; Brücher, E. Complexation Properties of the Di-, Tri-, and Tetraacetate Derivatives of Bis(Aminomethyl)Phosphinic Acid. *Eur. J. Inorg. Chem.* **2007**, *2007* (5), 701−713.

(68) Yoon, J.; Solomon, E. I. Electronic Structures of Exchange Coupled Trigonal Trimeric Cu(II) Complexes: Spin Frustration, Antisymmetric Exchange, Pseudo-A Terms, and Their Relation to O_2 Activation in the Multicopper Oxidases. *Coord. Chem. Rev.* **2007**, *251* (3−4), 379−400.

(69) Bataille, T.; Costantino, F.; Ienco, A.; Guerri, A.; Marmottini, F.; Midollini, S. A Snapshot of a Coordination Polymer Self-Assembly Process: The Crystallization of a Metastable 3D Network Followed by the Spontaneous Transformation in Water to a 2D Pseudopolymorphic Phase. *Chem. Commun.* **2008**, *47*, 6381−6383.

(70) Bataille, T.; Costantino, F.; Lorenzo-Luis, P.; Midollini, S.; Orlandini, A. A New Copper(II) Tubelike Metal−Organic Framework Constructed from P,P′-Diphenylmethylenediphosphinic Acid and 4,4′-Bipyridine: Synthesis, Structure, and Thermal Behavior. *Inorg. Chim. Acta* **2008**, *361* (1), 9−15.

(71) Costantino, F.; Ienco, A.; Midollini, S.; Orlandini, A.; Sorace, L.; Vacca, A. Copper(II) Complexes with Bridging Diphosphinates − The Effect of the Elongation of the Aliphatic Chain on the Structural Arrangements Around the Metal Centres. *Eur. J. Inorg. Chem.* **2008**, *2008* (19), 3046−3055.

(72) Costantino, F.; Ienco, A.; Midollini, S. Different Structural Networks Determined by Variation of the Ligand Skeleton in Copper(II) Diphosphinate Coordination Polymers. *Cryst. Growth Des.* **2010**, *10* (1), 7−10.

(73) Pothiraja, R.; Sathiyendiran, M.; Steiner, A.; Murugavel, R. Copper Phosphates and Phosphinates with Pyridine/Pyrazole Alcohol Co-Ligands: Synthesis and Structure. *Inorg. Chim. Acta* **2011**, *372* (1), 347−352.

(74) Liu, M. J.; Cao, D. K.; Liu, B.; Li, Y. Z.; Huang, J.; Zheng, L. M. Cobalt and Copper Phosphinates Based on N-(Phosphinomethyl)-Iminodiacetic Acid: Supramolecular Layered Structures and Magnetic Properties. *CrystEngComm* **2012**, *14* (14), 4699−4705.

(75) Taddei, M.; Ienco, A.; Costantino, F.; Guerri, A. Supramolecular Interactions Impacting on the Water Stability of Tubular Metal−Organic Frameworks. *RSC Adv.* **2013**, *3* (48), 26177−26183.

(76) Zhao, C. C.; Zhou, Z. G.; Xu, X.; Dong, L. J.; Xu, G. H.; Du, Z. Y. Isomerism of a Series of Octahedrally Coordinated Transition Metal Carboxylate−Phosphinates with 1,10-Phenanthroline as a Coligand: Discrete Dimers or Double-Chains Constructed by Various Dimeric Ring Motifs. *Polyhedron* **2013**, *51* (1), 18−26.

(77) Bronzan-Planinić, P.; Meider, H. Synthesis and Characterization of Cobalt(II), Nickel(II) and Copper(II) Perchlorate Complexes with Bis [(Diphenylphosphinyl)Methyl] Phenylphosphine Oxide, Bis [(Disphenylphosphinyl)Methyl]Ethyl Phosphinate, and Bis [(Diphenylphosphinyl)Methyl] Phosphinic. *Polyhedron* **1983**, *2* (2), 69−75.

(78) David, T.; Procházková, S.; Kotek, J.; Kubíček, V.; Hermann, P.; Lukeš, I. Aminoalkyl-1,1-Bis(Phosphinic Acids): Stability, Acid−Base, and Coordination Properties. *Eur. J. Inorg. Chem.* **2014**, *2014* (26), 4357−4368.

(79) Ienco, A.; Caporali, M.; Costantino, F.; Guerri, A.; Manca, G.; Moneti, S.; Peruzzini, M. The Quest for Hydrogen Bond-Based Metal Organic Nanotubes (MONT). *J. Coord. Chem.* **2014**, *67* (23−24), 3863−3872.

(80) Calancea, S.; Reis, S. G.; Guedes, G. P.; Cassaro, R. A. A.; Semaan, F.; López-Ortiz, F.; Vaz, M. G. F. A New Family of Multinuclear Mixed-Ligand Copper(II) Clusters: Crystal Structures, Magnetic Properties and Catecholase-like Activity. *Inorg. Chim. Acta* **2016**, *453*, 104−114.

(81) Li, J.; Xue, C.-C.; Liu, S.; Wang, Z.-X. Structures and Magnetic Properties of Two Noncentrosymmetric Coordination Polymers Based on Carboxyphosphinate Ligand. *Solid State Sci.* **2016**, *61*, 111−115.

(82) Beil, A.; Müller, G.; Käser, D.; Hattendorf, B.; Li, Z.; Krumeich, F.; Rosenthal, A.; Rana, V. K.; Schönberg, H.; Benkő, Z.; Grützmacher, H. Bismesitoylphosphinic Acid (BAPO-OH): A Ligand for Copper Complexes and Four-Electron Photoreductant for the Preparation of Copper Nanomaterials. *Angew. Chemie Int. Ed.* **2018**, *57* (26), 7697−7702.

(83) Hlinová, V.; Jaroš, A.; David, T.; Císařová, I.; Kotek, J.; Kubíček, V.; Hermann, P. Complexes of Phosphonate and Phosphinate Derivatives of Dipicolylamine. *New J. Chem.* **2018**, *42* (10), 7713−7722.

(84) Yang, Y. Y.; He, M. Q.; Li, M. X.; Huang, Y. Q.; Chi, T.; Wang, Z. X. Ferrimagnetic Copper-Carboxyphosphinate Compounds for Catalytic Degradation of Methylene Blue. *Inorg. Chem. Commun.* **2018**, *94*, 5−9.

(85) Ienco, A.; Tuci, G.; Guerri, A.; Costantino, F. Mechanochemical Access to Elusive Metal Diphosphinate Coordination Polymer. *Crystals* **2019**, *9* (6), 283.

(86) Gholivand, K.; Fallah, N.; Ebrahimi Valmoozi, A. A.; Gholami, A.; Dusek, M.; Eigner, V.; Pooyan, M.; Mohammadpanah, F. Synthesis and Structural Characterization of Phosphinate Coordination Polymers with Tin(IV) and Copper(II). *J. Mol. Struct.* **2020**, *1202*, No. 127369.

(87) Mohammadnezhad, G.; Amirian, A. M.; Görls, H.; Plass, W.; Sandleben, A.; Schäfer, S.; Klein, A. Redox Instability of Copper(II) Complexes of a Triazine-Based PNP Pincer. *Eur. J. Inorg. Chem.* **2021**, *2021* (12), 1140−1151.

(88) Haynes, J. S.; Oliver, K. W.; Rettig, S. J.; Thompson, R. C.; Trotter, J. Structure and Magnetic Exchange in Poly-Bis((μ-Dialkylphosphinato)Copper(II) Compounds. *Can. J. Chem.* **1984**, *62* (5), 891−898.

(89) Głowiak, T. Structure of Catena-Bis[μ-(Aminomethyl)-Methylphosphinato-N,O:O'-μ-Chloro-Copper(II)]. *Acta Crystallogr. Sect. C Cryst. Struct. Commun.* **1986**, *42* (1), 62−64.

(90) Bino, A.; Sissman, L. Preparation and Structure of Poly-Bis(μ-Diphenyl-Phosphinato)Copper(II). *Inorg. Chim. Acta* **1987**, *128* (2), L21−L22.

(91) Betz, P.; Bino, A. A New Class of Metalphosphinates Containing Bridging Formamide Ligands. *Inorg. Chim. Acta* **1988**, *149* (2), 171−175.

(92) Betz, P.; Bino, A. Crystal Structure of Poly-Bis(μ-Phenylmethylphosphinato)Copper(II)(Dimethylformamide). *Inorg. Chim. Acta* **1988**, *145* (1), 11−12.

(93) Rohovec, J.; Lukeš, I.; Vojtíšek, P.; Císařová, I.; Hermann, P. Complexing Properties of Phosphinic Analogues of Glycine. *J. Chem. Soc. Dalt. Trans.* **1996**, *13*, 2685−2691.

(94) Cole, E.; Parker, D.; Ferguson, G.; Gallagher, J. F.; Kaitner, B. Synthesis and Structure of Chiral Metal Complexes of Polyazacycloalkane Ligands Incorporating Phosphinic Acid Donors. *J. Chem. Soc. Chem. Commun.* **1991**, No. 20, 1473.

(95) Cole, E.; Copley, R. C. B.; Howard, J. A. K.; Parker, D.; Ferguson, G.; Gallagher, J. F.; Kaitner, B.; Harrison, A.; Royle, L. 1,4,7-Triazacyclononane-1,4,7-Triyltrimethylenetris-(Phenylphosphinate) Enforces Octahedral Geometry: Crystal and Solution Structures of Its Metal Complexes and Comparative Biodistribution Studies of Radiolabelled Indium and Gallium Complexes. *J. Chem. Soc. Dalton Trans.* **1994**, No. 11, 1619.

(96) David, T.; Kubíček, V.; Gutten, O.; Lubal, P.; Kotek, J.; Pietzsch, H.-J.; Rulíšek, L.; Hermann, P. Cyclam Derivatives with a Bis-(Phosphinate) or a Phosphinato−Phosphonate Pendant Arm: Ligands for Fast and Efficient Copper(II) Complexation for Nuclear Medical Applications. *Inorg. Chem.* **2015**, *54* (24), 11751−11766.

(97) Procházková, S.; Kubíček, V.; Böhmová, Z.; Holá, K.; Kotek, J.; Hermann, P. DOTA Analogues with a Phosphinate-Iminodiacetate Pendant Arm: Modification of the Complex Formation Rate with a Strongly Chelating Pendant. *Dalt. Trans.* **2017**, *46* (31), 10484−10497.

(98) Weekes, D. M.; Jaraquemada-Peláez, M. D. G.; Kostelnik, T. I.; Patrick, B. O.; Orvig, C. Di- and Trivalent Metal-Ion Solution Studies with the Phosphinate-Containing Heterocycle DEDA-(PO). *Inorg. Chem.* **2017**, *56* (17), 10155−10161.

(99) Paúrová, M.; David, T.; Císařová, I.; Lubal, P.; Hermann, P.; Kotek, J. Optimization of the Selectivity and Rate of Copper Radioisotope Complexation: Formation and Dissociation Kinetic Studies of 1,4,8-Trimethylcyclam-Based Ligands with Different

Coordinating Pendant Arms. *New J. Chem.* **2018**, *42* (14), 11908−11929.

(100) Pazderová, L.; Kubíček, V.; Kotek, J.; Hermann, P. 1,4,7-Triazacyclononane (Tacn) with N,N′-bridging Methylene-bis-(Phosphinic Acid) Group and Its Complexes. *Z. Anorg. Allg. Chem.* **2021**, *647* (12), 1261−1268.

(101) Pazderová, L.; David, T.; Kotek, J.; Kubíček, V.; Hermann, P. Complexes of Cyclen Side-Bridged with a Methylene-Bis(Phosphinate) Group. *Polyhedron* **2021**, *196*, No. 114994.

(102) Yamamoto, T.; Shimoda, A.; Okuhara, T.; Misono, M. A Promoting Effect of Phosphorus-Addition to Cu/SiO$_2$ on Selective Synthesis of Formaldehyde by Dehydrogenation of Methanol. *Chem. Lett.* **1988**, *17* (2), 273−276.

(103) Qi, X.; Zhang, L.; Xie, W.; Ji, T.; Li, R. Synthesis of Copper-Substituted Aluminophosphate Molecular Sieves (CuAPO-11) and Their Catalytic Behavior for Phenol Hydroxylation. *Appl. Catal. A Gen.* **2004**, *276* (1−2), 89−94.

(104) Siva Kumar, V.; Padmasri, A. H.; Satyanarayana, C. V. V.; Ajit Kumar Reddy, I.; David Raju, B.; Rama Rao, K. S. Nature and Mode of Addition of Phosphate Precursor in the Synthesis of Aluminum Phosphate and Its Influence on Methanol Dehydration to Dimethyl Ether. *Catal. Commun.* **2006**, *7* (10), 745−751.

(105) van der Bij, H. E.; Weckhuysen, B. M. Phosphorus Promotion and Poisoning in Zeolite-Based Materials: Synthesis, Characterisation and Catalysis. *Chem. Soc. Rev.* **2015**, *44* (20), 7406−7428.

(106) Xia, W.; Huang, Y.; Ma, C.; Li, S.; Wang, X.; Chen, K.; Liu, D. Multiple Important Roles of Phosphorus Modification on the ZSM-5 in Ethanol to Olefin Reaction: Acidity Adjustment, Hydrothermal Stability and Anti-Coking. *Fuel* **2023**, *341*, No. 127675.

(107) Schneider, C. A.; Rasband, W. S.; Eliceiri, K. W. NIH Image to ImageJ: 25 Years of Image Analysis. *Nat. Methods* **2012**, *9* (7), 671−675.

(108) Hooft, R. W. W. *Collect: Data Collection Software*; Nonius BV: Delft, 1998.

(109) Otwinowski, Z.; Minor, W. Processing of X-Ray Diffraction Data Collected in Oscillation Mode. *Methods Enzymol.* **1993**, *1997* (276), 307−326.

(110) Sheldrick, G. M. *SADABS-Bruker Nonius Scaling and Absorption Correction*; Bruker AXS Inc.: Madison, Wisconsin, USA, 2003.

(111) Sheldrick, G. M. SHELXT − Integrated Space-Group and Crystal-Structure Determination. *Acta Crystallogr. Sect. A Found. Adv.* **2015**, *71* (1), 3−8.

(112) Sheldrick, G. M. Crystal Structure Refinement with SHELXL. *Acta Crystallogr. Sect. C Struct. Chem.* **2015**, *71* (1), 3−8.

(113) Llunell, M.; Casanova, D.; Cirera, J.; Alemany, P.; Alvarez, S. *Users Manual: SHAPE. Program for the Stereochemical Analysis of Molecular Fragments by Means of Continuous Shape Measures and Associated Tools*, 2013.

(114) Pinsky, M.; Avnir, D. Continuous Symmetry Measures. 5. The Classical Polyhedra. *Inorg. Chem.* **1998**, *37* (21), 5575−5582.

(115) Cirera, J.; Alemany, P.; Alvarez, S. Mapping the Stereochemistry and Symmetry of Tetracoordinate Transition-Metal Complexes. *Chem.—Eur. J.* **2004**, *10* (1), 190−207.

(116) Alvarez, S.; Llunell, M. Continuous Symmetry Measures of Penta-Coordinate Molecules: Berry and Non-Berry Distortions of the Trigonal Bipyramid. *J. Chem. Soc. Dalt. Trans.* **2000**, *19*, 3288−3303.

(117) Robertson, B. E.; Calvo, C. The Crystal Structure and Phase Transformation of α-Cu$_2$P$_2$O$_7$. *Acta Crystallogr.* **1967**, *22* (5), 665−672.

(118) Eysel, W.; Wetzel, A. ICDD Grant-in-Aid. *Mineral.-Petrogr*; Institut, University Heidelberg: Germany. 1992.

(119) Schneider, M.; Trommer, J.; Wilde, L.; Fratzky, D. *ICDD Grant-in-Aid*; Inst. f. Angewandte Chemie: Berlin, Germany. 1999. https://www.icdd.com/grant-in-aid/.

(120) Forsyth, J. B.; Wilkinson, C.; Paster, S.; Effenberger, H. The Antiferromagnetic Structure of Triclinic Copper(II) Phosphate. *J. Phys.: Condens. Matter* **1990**, *2* (6), 1609−1617.

(121) Langford, J. I.; Louër, D. High-Resolution Powder Diffraction Studies of Copper(II) Oxide. *J. Appl. Crystallogr.* **1991**, *24* (2), 149−155.

(122) Campisano, I. S. P.; Rodella, C. B.; Sousa, Z. S. B.; Henriques, C. A.; Teixeira da Silva, V. Influence of Thermal Treatment Conditions on the Characteristics of Cu-Based Metal Oxides Derived from Hydrotalcite-like Compounds and Their Performance in Bio-Ethanol Dehydrogenation to Acetaldehyde. *Catal. Today* **2018**, *306*, 111−120.

(123) Amokrane, S.; Boualouache, A.; Simon, P.; Capron, M.; Otmanine, G.; Allam, D.; Hocine, S. Effect of Adding Transition Metals to Copper on the Dehydrogenation Reaction of Ethanol. *Catal. Lett.* **2021**, *151* (10), 2864−2883.

(124) Shard, A. G. Detection Limits in XPS for More than 6000 Binary Systems Using Al and Mg Kα X-Rays. *Surf. Interface Anal.* **2014**, *46* (3), 175−185.

(125) Biesinger, M. C.; Hart, B. R.; Polack, R.; Kobe, B. A.; Smart, R. S. C. Analysis of Mineral Surface Chemistry in Flotation Separation Using Imaging XPS. *Miner. Eng.* **2007**, *20* (2), 152−162.

(126) Zhang, H.; Tan, H.-R.; Jaenicke, S.; Chuah, G.-K. Highly Efficient and Robust Cu Catalyst for Non-Oxidative Dehydrogenation of Ethanol to Acetaldehyde and Hydrogen. *J. Catal.* **2020**, *389*, 19−28.

(127) Swanson, H. E.; Tatge, E. Standard X-Ray Diffraction Powder Patterns. *Natl. Bur. Stand. (U.S.), Circ.* **1953**, *539* (I), 31−32.

(128) Yu, J.; Yang, M.; Zhang, J.; Ge, Q.; Zimina, A.; Pruessmann, T.; Zheng, L.; Grunwaldt, J.; Sun, J. Stabilizing Cu$^+$ in Cu/SiO$_2$ Catalysts with a Shattuckite-Like Structure Boosts CO$_2$ Hydrogenation into Methanol. *ACS Catal.* **2020**, *10* (24), 14694−14706.

(129) Ivanova, T. M.; Maslakov, K. I.; Sidorov, A. A.; Kiskin, M. A.; Linko, R. V.; Savilov, S. V.; Lunin, V. V.; Eremenko, I. L. XPS Detection of Unusual Cu(II) to Cu(I) Transition on the Surface of Complexes with Redox-Active Ligands. *J. Electron Spectrosc. Relat. Phenom.* **2020**, *238*, 146878.

(130) Post, P.; Wurlitzer, L.; Maus-Friedrichs, W.; Weber, A. Characterization and Applications of Nanoparticles Modified in-Flight with Silica or Silica-Organic Coatings. *Nanomaterials* **2018**, *8*, 530.

(131) Wu, X.; Gong, K.; Zhao, G.; Lou, W.; Wang, X.; Liu, W. Mechanical Synthesis of Chemically Bonded Phosphorus−Graphene Hybrid as High-Temperature Lubricating Oil Additive. *RSC Adv.* **2018**, *8* (9), 4595−4603.

(132) Mitchell, D. F.; Clark, K. B.; Bardwell, J. A.; Lennard, W. N.; Massoumi, G. R.; Mitchell, I. V. Film Thickness Measurements of SiO$_2$ by XPS. *Surf. Interface Anal.* **1994**, *21* (1), 44−50.

(133) Styskalik, A.; Kordoghli, I.; Poleunis, C.; Delcorte, A.; Aprile, C.; Fusaro, L.; Debecker, D. P. Highly Porous Hybrid Metallosilicate Materials Prepared by Non-Hydrolytic Sol-Gel: Hydrothermal Stability and Catalytic Properties in Ethanol Dehydration. *Microporous Mesoporous Mater.* **2020**, *297*, No. 110028.

(134) Janvelyan, N.; Van Spronsen, M. A.; Wu, C. H.; Qi, Z.; Montemore, M. M.; Shan, J.; Zakharov, D. N.; Xu, F.; Boscoboinik, J. A.; Salmeron, M. B.; Stach, E. A.; Flyztani-Stephanopoulos, M.; Biener, J.; Friend, C. M. Stabilization of a Nanoporous NiCu Dilute Alloy Catalyst for Non-Oxidative Ethanol Dehydrogenation. *Catal. Sci. Technol.* **2020**, *10* (15), 5207−5217.

(135) Kumar, A.; Bal, R.; Srivastava, R. Modulation of Ru and Cu Nanoparticle Contents over CuAlPO-5 for Synergistic Enhancement in the Selective Reduction and Oxidation of Biomass-Derived Furan Based Alcohols and Carbonyls. *Catal. Sci. Technol.* **2021**, *11* (12), 4133−4148.

(136) Sepúlveda, C.; Delgado, L.; García, R.; Melendrez, M.; Fierro, J. L. G.; Ghampson, I. T.; Escalona, N. Effect of Phosphorus on the Activity of Cu/SiO$_2$ Catalysts in the Hydrogenolysis of Glycerol. *Catal. Today* **2017**, *279*, 217−223.

(137) Pamparraro, G.; Garbarino, G.; Riani, P.; Villa García, M.; Sánchez Escribano, V.; Busca, G. A Study of Ethanol Dehydrogenation to Acetaldehyde over Supported Copper Catalysts: Catalytic Activity, Deactivation and Regeneration. *Appl. Catal. A Gen.* **2020**, *602*, No. 117710.